





# The open cluster NGC 2345: a study of chemical abundances with near-infrared IGRINS high-resolution spectra

N. Holanda <sup>1</sup>★, M. P. Roriz <sup>1</sup>, N. A. Drake <sup>1,2</sup>, S. Junqueira,<sup>1</sup> S. Daflon <sup>1</sup>, J. R. P. da Silva<sup>3</sup> and C. B. Pereira<sup>1</sup>

<sup>1</sup>Observatório Nacional, Rua General José Cristino 77, 20921-400, São Cristóvão, Rio de Janeiro, RJ, Brazil

<sup>2</sup>Laboratory of Observational Astrophysics, Saint Petersburg State University, Universitetski pr. 28, 198504 Saint Petersburg, Russia

<sup>3</sup>Universidade do Estado do Rio Grande do Norte, Departamento de Física, Rua Prof. Antonio Campos, 59610-090 Mossoró, Brazil

Accepted 2023 October 23. Received 2023 September 28; in original form 2023 June 1

## ABSTRACT

Open clusters are relatively young and numerous. These systems are distributed throughout the Galactic disc and provide insights on the chemistry of the Milky Way. In this study, we provide a near-infrared spectroscopic analysis of four stars of the young open cluster NGC 2345. Our infrared data present a resolving power of  $R \approx 45\,000$ , covering the *H*- and *K*-bands ( $1.5\text{--}2.5\ \mu\text{m}$ ), and high-signal-to-noise ratio, which are gathered with the Immersion Grating Infrared Spectrograph (IGRINS) at the Gemini Observatory. From atmospheric parameters previously derived via optical spectroscopy, we obtain abundances for C ( $^{12}\text{C}/^{16}\text{O}$ ), N ( $^{12}\text{C}/^{14}\text{N}$ ), O ( $^{16}\text{O}$ ), F ( $\text{H}^{19}\text{F}$ ), Na, Mg, Al, Si, P, S, K, Ca, Sc, Ti, Cr, Fe, Ni, Ce, Nd, and Yb. Additionally, the  $^{12}\text{C}/^{13}\text{C}$  ( $^{13}\text{C}/^{16}\text{O}$ ),  $^{16}\text{O}/^{17}\text{O}$  ( $^{12}\text{C}/^{17}\text{O}$ ), and  $^{16}\text{O}/^{18}\text{O}$  ( $^{12}\text{C}/^{18}\text{O}$ ) isotopic ratios are obtained. We compare the infrared results with a previous work based on optical spectral analysis, but chemical species such as F, S, P, K, and Yb are determined for the first time in stars of NGC 2345. We also confirm a low metallicity ( $[\text{Fe}/\text{H}] = -0.32 \pm 0.04$ ) and slight enrichment in *s*-process elements, as already noticed in works available in the literature, but we do not find any enrichment in F. Our results demonstrate excellent agreement between our measured isotopic ratios  $^{12}\text{C}/^{13}\text{C}$  and  $^{16}\text{C}/^{17}\text{O}$  and models of stellar nucleosynthesis, while we find that the abundance of  $^{18}\text{O}$  is overestimated in comparison to our measurements. Finally, we assess our findings in comparison to the chemical patterns observed in open clusters, classified by both their age and Galactocentric distances, and highlight the need for a more comprehensive sample of young clusters within the 9–11 kpc range for a proper comparison.

**Key words:** techniques: spectroscopic – stars: abundances – stars: fundamental parameters – (Galaxy:) open clusters and associations: individual: NGC 2345.

## 1 INTRODUCTION

Open clusters are groups of stars gravitationally bound and located at the same distance, with similar age and initial chemical composition. These clusters are valuable tracers of the Galactic chemical properties because they are distributed throughout the disc. Many authors refer to them as ‘laboratories’ for studies in the scope of Galactic chemical evolution and stellar evolution (e.g. Friel 1995; Lada & Lada 2003; Netopil et al. 2016; Krumholz, McKee & Bland-Hawthorn 2019).

Spectroscopy technique applied to high-quality data, i.e. high-resolution optical (OP) spectra, can provide impressive abundance results for a large variety of chemical species, and their applications are wide; studies on stellar populations, chemical history of the Galaxy, and nuances of stellar evolution, including chemically peculiar stars, are some examples (e.g. Pereira et al. 2019; Holanda, Drake & Pereira 2020a, b). However, by combining spectroscopic data in different domains such as OP and near-infrared (NIR), analytical challenges can be faced; furthermore, chemical abundance for the same element

can be derived from different spectral regions, and better constraints on stellar parameters can be found as well. In other words, NIR spectral investigation can provide reliable abundances for chemical elements with some methodical difficulties in the OP spectra window; for instance, contamination of the [OI] line by telluric lines, an important line (traditionally) used to determine oxygen abundance (e.g. Afşar et al. 2016, 2018; Böcek Topcu et al. 2019, 2020).

NIR spectra of (super) red giants offer a wealth of information. Their spectra contain strong absorption features and molecular bands, such as CO, that are highly sensitive to the star’s atmospheric conditions. Consequently, we can determine stellar effective temperature and surface gravity, as demonstrated by studies such as of Park et al. (2018). Furthermore, the carbon and oxygen isotopic ratios ( $^{12}\text{C}/^{13}\text{C}$ ,  $^{16}\text{C}/^{17}\text{O}$ , and  $^{16}\text{C}/^{18}\text{O}$ ) derived from NIR spectra provide insights into stellar evolution and act as tracers of (extra) mixing (Harris, Lambert & Smith 1988; Tsuji 2008; Lebzelter et al. 2015; Guerço et al. 2022).

The NGC 2345 cluster is well studied in the OP domain, and there is a consistency of results regarding its ‘low’ metallicity. Four previous studies of the stars from NGC 2345 reported a low mean metallicity (Reddy, Lambert & Giridhar 2016; Alonso-Santiago et al.

\* E-mail: [nacizoholanda@on.br](mailto:nacizoholanda@on.br)

**Table 1.** Basic information of the observed stars in NGC 2345.

Star	Gaia ID (DR2)	RA (J2000)	Dec (J2000)	Type <sup>a</sup>	V <sup>b</sup> (mag)	K <sup>c</sup> (mag)	H <sup>c</sup> (mag)	Date yy mm dd	Remarks <sup>d</sup>
#14	3 044 668 888 404 742 528	07 08 17.46	−13 11 30.49	K2 II	10.754	5.799	5.503	2021 Oct 01	Single
#43	3 044 669 232 011 557 760	07 08 26.32	−13 11 14.44	—	10.717	6.474	6.157	2021 Oct 04	Single
#50	3 044 666 242 714 331 008	07 08 27.01	−13 12 32.98	K2 II	10.288	5.479	6.174	2021 Oct 27	Single
#60	3 044 665 967 836 430 976	07 08 30.37	−13 13 52.55	K3 II	10.480	6.246	5.965	2021 Oct 27	Single

Sources: <sup>a</sup>Skiff (2014); <sup>b</sup>Zacharias et al. (2013); <sup>c</sup>Cutri et al. (2003); and <sup>d</sup>Mermilliod, Mayor & Udry (2008).

2019; Holanda, Pereira & Drake 2019; Carrera et al. 2022) despite its young age (56 to 208 Myr; Reddy, Lambert & Giridhar 2016; Alonso-Santiago et al. 2019; Cantat-Gaudin et al. 2020), Galactocentric distance (9.88 to 10.22 kpc; Alonso-Santiago et al. 2019; Holanda et al. 2019; Cantat-Gaudin et al. 2020), and low Galactic latitude. Among these studies, the work conducted by Holanda et al. (2019; referred to as H19) stands out. H19 employed high-resolution OP spectra to determine atmospheric parameters, abundances for 20 chemical species, and the <sup>12</sup>C/<sup>13</sup>C ratios for five evolved stars (#14, #34, #43, #50, and #60). It is noteworthy that one of these stars (#34) is part of a spectroscopic binary system and exhibits a high projected rotational velocity.

Our group conducted a series of chemical studies of stars in open clusters, as evidenced by previous studies (e.g. Martinez et al. 2020; Holanda et al. 2021, 2022). This paper presents new research focusing on the NIR domain for four stars previously analysed with OP spectra (#14, #43, #50, and #60; Table 1). We re-determined a set of abundances using NIR spectra and provided for the first time a set of abundances for stars in NGC 2345. The paper is structured in the following manner: We describe the observations, data analysis, effective temperature calibrations, and abundance determinations in Section 2, along with the atomic and molecular data used in abundance determinations. In Section 3, we discuss the results and provide tests of equivalent width calibrations, mixing models, and the relations between abundance, age, and Galactocentric distances for open clusters. We compare our results with abundances of giant and dwarf stars of the Galactic thin disc to better describe our sample. Finally, we summarize the results in Section 4.

## 2 OBSERVATIONS AND ANALYSIS

### 2.1 Spectroscopic data

The observations were carried out using the Immersion GRating Infrared Spectrometer (IGRINS; Yuk et al. 2010) on the 8.1 m Gemini-South telescope at Cerro Pachón, Chile, by proposal GS-2021B-Q-301 (P.I. Nacizo Holanda) submitted to Laboratório Nacional de Astrofísica. The IGRINS is a cross-dispersed NIR spectrograph with a resolving power of  $R \approx 45\,000$  that covers the *H*- (14 900–18 000 Å) and *K*-bands (19 600–24 600 Å), providing broad spectral coverage and high spectral resolution. The targets were observed using an ABBA nod sequence along the slit, employing exposure times to ensure spectra with a high signal-to-noise ratio ( $S/N \geq 150$ ). The data reduction process involved utilizing the IGRINS pipeline package, PLP2.<sup>1</sup> Within the pipeline framework, the spectra underwent essential procedures, including telluric correction, wavelength calibration, and flat-field correction. A telluric correction

<sup>1</sup>The PLP2 has been developed by the team led by Jae-Joon Lee at Korea Astronomy and Space Science Institute and by Soojong Pak at Kyung Hee University (previous version). It is available on: <https://github.com/igrins/plp>.

was performed by observing an AOV-type standard star with a similar airmass as the science target. The observed telluric standard star spectrum is scaled to match the science target spectrum’s continuum shape and then divided by it to remove atmospheric absorption features.

### 2.2 Atmospheric parameters

The atmospheric parameters – effective temperature ( $T_{\text{eff}}$ ), surface gravity ( $\log g$ ), microturbulent velocity ( $\xi_t$ ), and metallicity ( $[\text{Fe}/\text{H}]$ ) – were obtained from Holanda et al. (2019), who determined these values using the standard spectral method (see Table 2). Specifically, they adopted a list of Fe I and Fe II lines that are sufficiently isolated to avoid line blending with CN bands. These parameters are consistent with values obtained by different authors using different line lists and spectral resolutions, such as Alonso-Santiago et al. (2019) and Carrera et al. (2022).

In this work, we present new  $T_{\text{eff}}$  values derived from IGRINS spectra using three supplementary methods widely used in OP spectra analysis: equivalent-width (EW) calibrations, line-depth ratios (LDR), and photometric temperatures based on ( $V - K$ ) colour. Accurate temperature estimates are crucial for obtaining correct physical parameters and reliable chemical abundances, as the strengths of absorption lines can depend on the temperature of the star’s photosphere. Therefore, we apply these additional methods to validate the  $T_{\text{eff}}$  values obtained using the conventional method.

#### 2.2.1 Effective temperature calibrations

Park et al. (2018) presented a library of IGRINS spectra composed of 84 stars. In that work, the authors also identified atomic and molecular lines sensitive to the  $T_{\text{eff}}$  and  $\log g$  parameters and presented an alternative method to derive such parameters without stellar atmospheric models. To construct an empirical set of EW calibrations, these authors classified the sample into luminosity classes and spectral types (applicable to  $T_{\text{eff}}$  ranges). Spectral absorption lines, such as Al I 16 720 and 21 170 Å, Na I 22 090 Å, Ti I 22 240 Å, and CO 22 930 Å can be used to obtain the temperature and surface gravity of stars of near-solar metallicity. We selected only the cleanest (unblended) and most easily measurable lines studied by Park et al. (2018) to estimate the effective temperature (16 720, 21 170, and 22 240 Å). The results are in excellent agreement with the effective temperature values obtained via standard spectral analysis (see Table 2).

Additionally, the LDRs method considers the ratios of depths of absorption lines with different low excitation potentials to estimate effective temperatures and is widely adopted to analyse OP spectra. In this sense, Fukue et al. (2015) derived temperature scales from LDR calibrations for high-resolution NIR spectra for (super) giants. They used a set of lines in the *H*-band and achieved high accuracy,

**Table 2.** Atmospheric parameters and  $v \sin i$  values for the sample. Alternative effective temperature values are determined via EW, LDR, and  $(V-K)$  colour calibrations (Alonso, Arribas & Martínez-Roger 1999; Fukue et al. 2015; Park et al. 2018). The estimated uncertainty for  $v \sin i$  is  $\leq 1 \text{ km s}^{-1}$ .

Star	$T_{\text{eff}}$ K	$\log g$ $\text{cm s}^{-1}$	$\xi_t$ $\text{km s}^{-1}$	[Fe I/H] dex	[Fe II/H] dex	$v \sin i$ $\text{km s}^{-1}$	$\langle T_{\text{eff, EW}} \rangle$ K	$\langle T_{\text{eff, LDR}} \rangle$ K	$T_{\text{eff, (V-K)}}$ K
#14	$4150 \pm 110$	$1.1 \pm 0.1$	$2.36 \pm 0.16$	$-0.33 \pm 0.09$	$-0.34 \pm 0.13$	4.5	$4155 \pm 156$	$4195 \pm 157$	$4158 \pm 33$
#43	$4350 \pm 80$	$1.6 \pm 0.1$	$2.45 \pm 0.17$	$-0.32 \pm 0.07$	$-0.31 \pm 0.07$	4.7	$4472 \pm 190$	$4405 \pm 228$	$4674 \pm 37$
#50	$4000 \pm 90$	$0.7 \pm 0.2$	$2.31 \pm 0.20$	$-0.37 \pm 0.10$	$-0.37 \pm 0.10$	5.2	$3966 \pm 169$	$4033 \pm 173$	$4246 \pm 34$
#60	$4020 \pm 80$	$1.0 \pm 0.2$	$2.54 \pm 0.19$	$-0.39 \pm 0.08$	$-0.38 \pm 0.10$	5.8	$4246 \pm 195$	$4339 \pm 130$	$4684 \pm 37$

Reference for  $T_{\text{eff}}$ ,  $\log g$ ,  $\xi_t$ , [Fe I, II/H], and  $v \sin i$ : Holanda et al. (2019).

which is better for stars with  $[\text{Fe}/\text{H}] \geq -0.3$ . Despite the NGC 2345 objects present metallicity near this limit, we applied their polynomials and compared the results with the spectroscopic values. We considered three pairs of the lines to compute the mean effective temperature for each star, which followed the criteria for absorption lines of the same element or pairs composed of elements with the same main astrophysical site ( $\text{Fe I}_{15194}/\text{Fe I}_{15207}$ ,  $\text{Ti I}_{15544}/\text{Fe I}_{15591}$ , and  $\text{Ti I}_{15603}/\text{Fe I}_{16041}$ ).

In addition, to derive the third set of temperature values, we used a traditional method based on the  $(V-K)$  colour index, which is the best temperature indicator for giant stars (Alonso et al. 1999). For this, we considered the relationship  $A_V/E(V-K) = 1.13$  (Cox 2000, and references therein) and adopted  $E(B-V) = 0.66$ , which is the average cluster reddening determined by Alonso-Santiago et al. (2019) from the likely members analysed by them.

In Table 1, we compiled the mean effective temperature values obtained using the three alternative methods. Comparing the alternative results with the spectroscopic effective temperature values, the EW and LDR calibrations show good concordance and can be an excellent alternative to obtain temperatures, independent of reddening and extinction effects (e.g. due to a lack of information, highly obscured stars, and large uncertainties or significant differential reddening). However, star #60 exhibited differences of 226 K and 319 K compared to the most reliable alternative methods, EW and LDR. These differences may potentially account for the discrepancies observed in the analysis of chemical abundances, as discussed in Section 3.

### 2.3 Abundance determination

In this analysis, we have considered a set of 20 chemical species that can be investigated with IGRINS spectral coverage. Their elemental abundances for the four target stars were derived exclusively by comparing observed and theoretical spectra (spectral synthesis). The synthetic spectra were computed by the line synthesis code MOOG (version 2013; Sneden 1973), which assumes the local thermodynamic equilibrium (LTE) conditions. The line lists used as input to generate the synthetic spectra were compiled from many sources of the literature, as we describe below.

For the light elements, we used rotational-vibrational transitions of CO molecules to derive the abundance of  $^{12}\text{C}$ , and the isotopes  $^{13}\text{C}$ ,  $^{17}\text{O}$ , and  $^{18}\text{O}$ , while the OH molecule was adopted to derive the abundance of  $^{16}\text{O}$ . The CO and OH lines are abundant in the NIR spectra of evolved stars, therefore we are able to analyse different regions in the  $H$ - and  $K$ -bands to obtain the mean abundance values. In addition, the nitrogen abundance was obtained by analysing the electronic transitions of  $^{12}\text{C}^{14}\text{N}$  ( $A^2\Pi-X^2\Sigma$ ). A similar procedure described by Smith et al. (2013) was adopted to solve the interdependence for these light species, as is summarized in the following:

first, we constraint the  $^{16}\text{O}$  abundance from the OH lines and fixed this value to estimate the  $^{12}\text{C}$  abundance from the synthesis of the  $^{12}\text{CO}$  line(s); later, the derived  $^{12}\text{C}$  abundance is adopted to find the final  $^{16}\text{O}$  abundance from the OH lines; with this new value fixed the spectral synthesis of the  $^{12}\text{CO}$  lines yields the final  $^{12}\text{C}$  abundance; finally, we determined  $^{14}\text{N}$  abundance from CN synthesis keeping the final  $^{16}\text{O}$  and  $^{12}\text{C}$  abundances fixed. The nitrogen abundance is little affected by the CO and OH lines since  $\text{C/O} \leq 1.0$ . For these molecules, we adopted the dissociation energy values  $D_0(\text{CO}) = 11.092 \text{ eV}$ ,  $D_0(\text{OH}) = 4.411 \text{ eV}$ , and  $D_0(\text{CN}) = 7.724 \text{ eV}$ . Fig. 1 showcases diverse examples of spectral synthesis for molecular and atomic lines.

The isotopic ratios  $^{12}\text{C}/^{13}\text{C}$  and  $^{16}\text{O}/^{17}\text{O}$ ,  $^{18}\text{O}$  were obtained using  $gf$ -values from Kurucz (2011). To determine the  $^{12}\text{C}/^{13}\text{C}$  ratio values, we analysed two regions containing the  $^{13}\text{C}^{16}\text{O}$  ( $2-0$ ) R49-56 and ( $3-1$ ) R46-R57 lines. The  $^{16}\text{O}/^{17}\text{O}$  ratio values were determined by synthesizing two regions with the  $^{12}\text{C}^{17}\text{O}$  ( $2-0$ ) R28 and R29 lines. In addition, the oxygen isotopic ratio  $^{16}\text{O}/^{18}\text{O}$  was determined using the  $^{12}\text{C}^{18}\text{O}$  ( $2-0$ ) R23 line. For clarity, Fig. 2 shows three examples.

The fluorine abundance was determined through analysis of the rotational-vibrational transition of  $\text{H}^{19}\text{F}$  ( $1-0$ ) R9, using a  $gf$ -value sourced from Jönsson et al. (2014). This specific line at  $23\,358 \text{ \AA}$ , is widely adopted in the literature for determining fluorine abundance in cool stars due to its prominence and relatively isolated nature, even in cases where significant fluorine enrichment is absent. However, it is important to recognize the diminished intensity of the HFR9 line with increasing temperature, which is a characteristic behaviour observed in certain molecular absorption lines within stellar spectra. In Fig. 3, we present the spectral region encompassing the HF line and showcase the fitting process of synthetic spectra to the observed spectra for a subset of the sample. Significantly, among these, the star #43, the warmest object in our sample, displays a less pronounced HF line compared to the other two stars. Conversely, the star #60 was excluded from the analysis due to its extremely low fluorine abundance, accompanied by an estimated uncertainty notably larger than that of the other stars within the sample. Fig. 3 illustrates the corrected spectra (represented as grey circles) following the removal of telluric lines (indicated by the green line). The blue line represents the observed spectrum before telluric lines were removed, describing the contaminated data, while the red line corresponds to the best-fitting synthetic spectra.

Chemical abundance for other species as Na I, Mg I, Al I, Si I, P I, S I, K I, Ca I, Sc I, Ti I, Cr I, Fe I, Ni I, Ce II, Nd II, and Yb II were determined via spectral synthesis of atomic lines. Much information was taken from Afşar et al. (2018; who used IGRINS spectra of giant stars and determined the astrophysical  $gf$ -values), Civiš et al. (2013), Kramida et al. (2014), Pehlivan, Nilsson & Hartman (2015), Hasselquist et al. (2016), and Cunha et al. (2017; see Appendix).

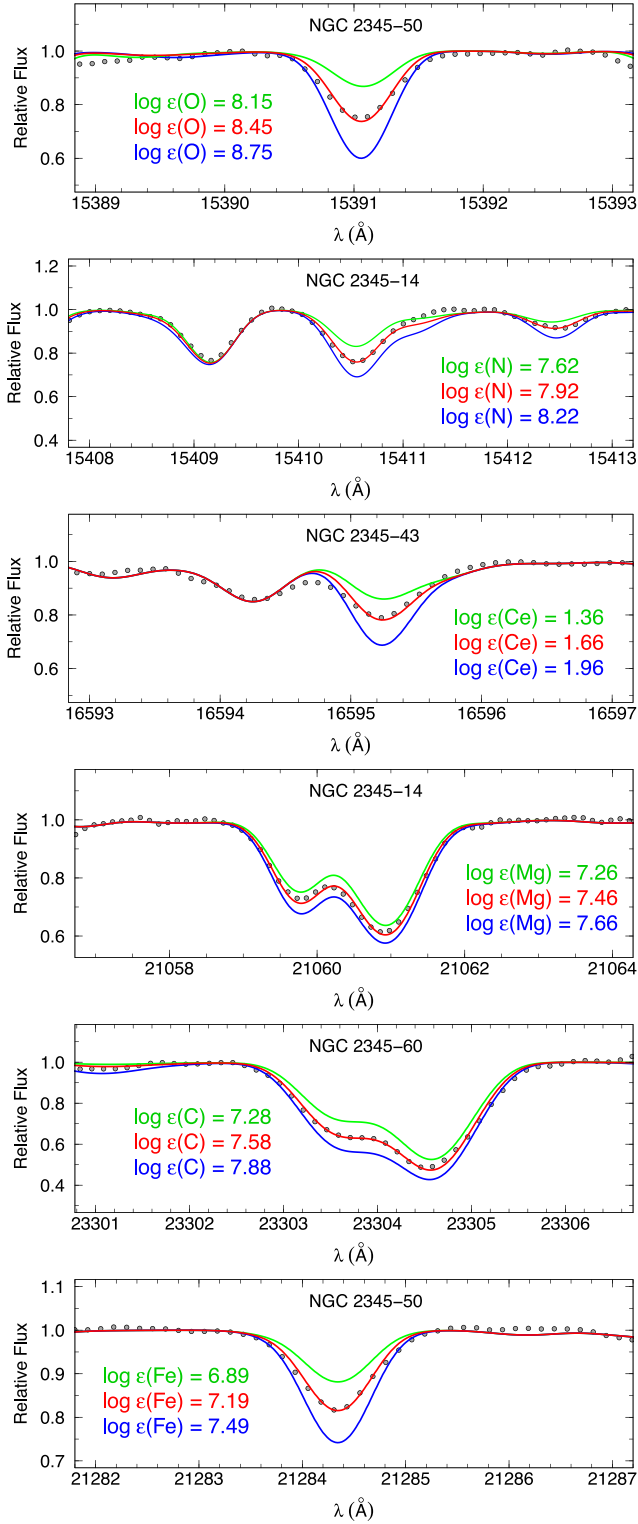


**Figure 1.** Best-fitting results obtained from synthetic spectra (red solid lines) and observed IGRINS spectra (grey circles) of stars. Additional lines are included to illustrate variations in abundance for the same spectral features.

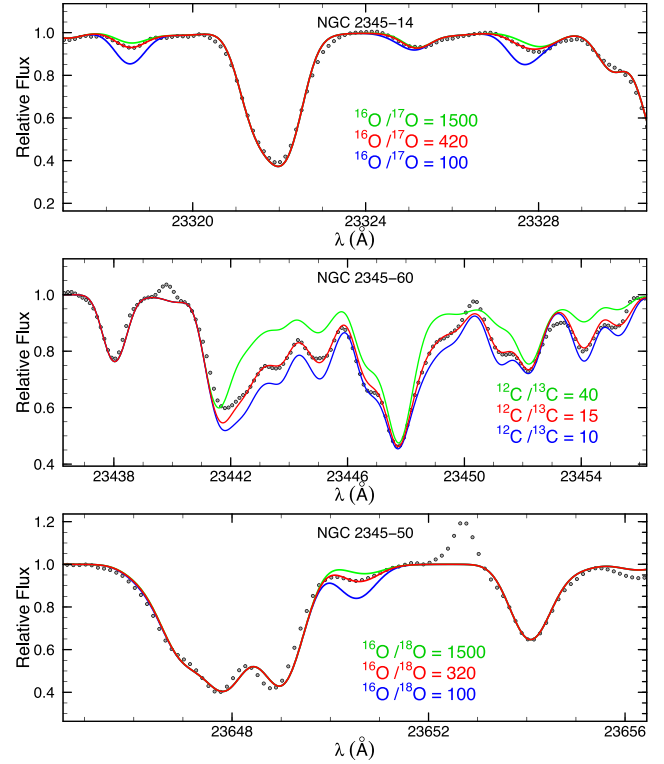


**Figure 2.** Spectral synthesis at 23 320 Å ( $^{12}\text{C}^{17}\text{O}$ ), 23 440 Å ( $^{13}\text{C}^{16}\text{O}$ ), and 23 650 Å ( $^{12}\text{C}^{18}\text{O}$ ) regions for the stars #14, #60, and #50, respectively. Red solid lines represent the best fit in each example.

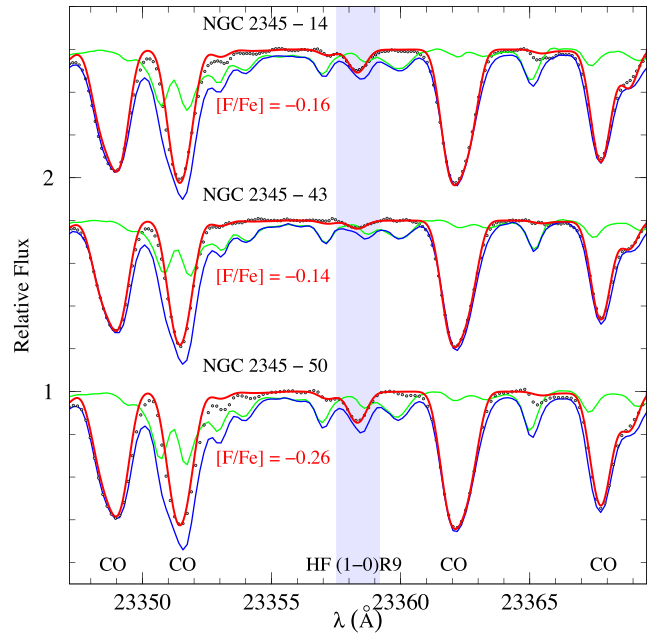


**Figure 3.** Spectral synthesis at 23 358 Å (HF). The grey dotted lines describe the corrected spectra in the vicinity of the HF line. Each star's best-fitting synthetic spectrum is represented by the red line, while the spectra containing telluric lines are shown in green. The blue line represents the spectra that include blending from both the star and telluric lines.

**Table 3.** Abundance ratios derived in this study and previous results reported by other works.

[X/Fe]	#14	#43	#50	#60	([X/Fe])	Ref.
C (CO; NIR)	-0.05 (03)	+0.06 (03)	-0.18 (03)	-0.38 (03)	-0.14 ± 0.19	This work
C (C <sub>2</sub> ; OP)	+0.02 (01)	+0.26 (01)	+0.11 (01)	+0.13 (01)	+0.13 ± 0.10	Holanda et al. (2019)
N (CN; NIR)	+0.35 (06)	+0.14 (06)	+0.44 (06)	+0.49 (06)	+0.35 ± 0.15	This work
N (CN; OP)	+0.62 (01)	+0.21 (01)	+0.51 (01)	+0.63 (01)	+0.49 ± 0.20	Holanda et al. (2019)
O (OH; NIR)	+0.16 (05)	+0.14 (05)	+0.10 (05)	-0.30 (05)	+0.02 ± 0.22	This work
F (HF; NIR)	-0.12 (01)	-0.14 (01)	-0.26 (01)	—	-0.17 ± 0.08	This work
Na I (NIR)	+0.39 (03)	+0.05 (03)	+0.39 (03)	+0.07 (03)	+0.22 ± 0.19	This work
Na I (OP)	+0.40 (03)	+0.10 (04)	+0.34 (03)	+0.21 (02)	+0.26 ± 0.13	Holanda et al. (2019)
Na I (OP)	—	+0.10	—	+0.38	+0.24 ± 0.20	Carrera et al. (2022)
Mg I (NLTE, NIR)	-0.01 (02)	0.00 (02)	-0.02 (02)	-0.02 (02)	-0.01 ± 0.01	This work
Mg I (NIR)	+0.11 (02)	+0.11 (02)	+0.10 (02)	+0.09 (02)	+0.10 ± 0.01	This work
Mg I (OP)	+0.09 (05)	+0.21 (03)	+0.26 (03)	+0.22 (04)	+0.19 ± 0.07	Holanda et al. (2019)
Mg I (OP)	—	-0.06	—	-0.03	-0.04 ± 0.02	Carrera et al. (2022)
Al I (NLTE, NIR)	+0.12 (02)	+0.01 (02)	+0.15 (02)	-0.19 (02)	+0.02 ± 0.15	This work
Al I (NIR)	+0.29 (02)	+0.18 (02)	+0.34 (02)	-0.02 (02)	+0.20 ± 0.16	This work
Al I (OP)	+0.17 (03)	+0.09 (04)	+0.13 (04)	+0.09 (05)	+0.12 ± 0.04	Holanda et al. (2019)
Al I (NLTE, OP)	+0.07 (03)	-0.03 (04)	+0.04 (04)	-0.04 (05)	+0.01 ± 0.05	Holanda et al. (2019)/This work
Al I (OP)	—	+0.10	—	+0.19	+0.14 ± 0.06	Carrera et al. (2022)
Si I (NIR)	+0.05 (04)	+0.02 (04)	+0.03 (05)	+0.01 (05)	+0.03 ± 0.02	This work
Si I (OP)	+0.28 (06)	+0.31 (01)	+0.28 (07)	+0.41 (04)	+0.32 ± 0.06	Holanda et al. (2019)
Si I (OP)	—	+0.05	—	+0.23	+0.14 ± 0.04	Carrera et al. (2022)
P I (NIR)	+0.32 (01)	+0.67 (01)	+0.53 (01)	+0.52 (01)	+0.51 ± 0.14	This work
S I (NIR)	+0.15 (03)	+0.18 (04)	+0.31 (04)	+0.42 (04)	+0.26 ± 0.12	This work
K I (NIR)	+0.31 (01)	+0.20 (01)	+0.27 (01)	+0.21 (01)	+0.25 ± 0.05	This work
Ca I (NIR)	+0.18 (04)	+0.08 (04)	+0.13 (04)	+0.05 (04)	+0.11 ± 0.06	This work
Ca I (OP)	-0.03 (03)	-0.03 (03)	+0.01 (02)	+0.02 (03)	-0.01 ± 0.03	Holanda et al. (2019)
Ca I (OP)	—	-0.04	—	-0.06	-0.05 ± 0.01	Carrera et al. (2022)
Sc I (NIR)	+0.09 (02)	-0.05 (02)	+0.13 (02)	-0.34 (02)	-0.04 ± 0.21	This work
Sc I (OP)	—	-0.15	—	-0.08	-0.11 ± 0.05	Carrera et al. (2022)
Ti I (NIR)	+0.13 (05)	+0.06 (05)	+0.23 (05)	-0.17 (05)	+0.06 ± 0.17	This work
Ti I (OP)	+0.00 (04)	-0.05 (07)	+0.08 (04)	—	+0.01 ± 0.07	Holanda et al. (2019)
Ti I (OP)	—	+0.03	—	+0.00	+0.01 ± 0.02	Carrera et al. (2022)
Cr I (NIR)	+0.11 (02)	+0.04 (02)	+0.11 (02)	-0.04 (02)	+0.05 ± 0.07	This work
Cr I (OP)	+0.06 (11)	+0.03 (15)	+0.03 (07)	-0.04 (07)	+0.02 ± 0.04	Holanda et al. (2019)
Cr I (OP)	—	-0.04	—	+0.00	-0.02 ± 0.03	Carrera et al. (2022)
Fe I* (NIR)	-0.28 (08)	-0.28 (08)	-0.34 (08)	-0.37 (08)	-0.32 ± 0.04	This work
Fe I* (OP)	-0.33 (14)	-0.32 (14)	-0.37 (13)	-0.39 (12)	-0.35 ± 0.03	Holanda et al. (2019)
Fe I* (OP)	—	-0.11	—	-0.23	-0.17 ± 0.08	Carrera et al. (2022)
Ni I (NIR)	+0.01 (04)	+0.01 (03)	+0.04 (03)	+0.13 (01)	+0.05 ± 0.06	This work
Ni I (OP)	-0.05 (06)	-0.06 (09)	-0.05 (11)	-0.06 (05)	-0.05 ± 0.01	Holanda et al. (2019)
Ni I (OP)	—	-0.16	—	-0.11	-0.13 ± 0.04	Carrera et al. (2022)
Ce II (NIR)	+0.28 (02)	+0.34 (02)	+0.13 (02)	+0.04 (02)	+0.20 ± 0.14	This work
Ce II (OP)	+0.28 (04)	+0.35 (04)	+0.21 (04)	+0.05 (06)	+0.25 ± 0.15	Holanda et al. (2019)
Ce II (OP)	—	+0.11	—	+0.15	+0.13 ± 0.03	Carrera et al. (2022)
Nd II (NIR)	+0.26 (02)	+0.36 (02)	+0.46 (01)	+0.43 (01)	+0.38 ± 0.09	This work
Nd II (OP)	+0.35 (05)	+0.41 (07)	+0.22 (08)	+0.20 (11)	+0.29 ± 0.10	Holanda et al. (2019)
Nd I (OP)	—	+0.10	—	+0.44	+0.27 ± 0.24	Carrera et al. (2022)
Yb II (NIR)	+0.22 (01)	+0.44 (01)	+0.35 (01)	+0.44 (01)	+0.36 ± 0.10	This work

Note. \*This ratio represents [Fe/H].

Additionally, the program LINEMAKE<sup>2</sup> (Placco et al. 2021) was used to construct all generic line-list inputs.

We have applied corrections to the magnesium and aluminum abundances, taking into account the substantial departure from LTE (NLTE) observed in late-type stars. To rectify this, we employed correction grids provided by Osorio et al. (2015) for Mg I and Nordlander & Lind (2017) for Al I lines. These corrections led to a mean difference of  $\langle \Delta \text{Mg} \rangle = -0.14$  dex and  $\langle \Delta \text{Al} \rangle = -0.18$  dex

in the derived abundances. Comprehensive individual corrections can be referenced in the Appendix.

All abundance results were normalized to the solar values provided by Asplund et al. (2009) and are given in Table 3.

### 2.3.1 Abundance uncertainties

We conducted a comprehensive analysis to assess the uncertainties in determining the chemical abundances for star #43, which serves as an illustrative example from the sample. Our analysis follows the methodology described in H19, allowing us to estimate the uncertainties associated with the atmospheric parameters. The error in  $T_{\text{eff}}$

<sup>2</sup>Available on <https://github.com/vmplacco/linemake>

**Table 4.** Abundance uncertainties for the star NGC 2345-43. From the second to the fifth column, we show the variations of abundances caused by the variations of the atmospheric parameters. In the last column, we present the total uncertainty of the second to the fifth columns.

$\log \varepsilon(X)$	$\Delta T_{\text{eff}}$ +80 K	$\Delta \log g$ +0.10 dex	$\Delta \log \varepsilon(\text{Fe})$ +0.07 dex	$\Delta \xi_t$ +0.17 dex	$\sigma_{\text{atm}}$
F (HF)	+0.12	0.00	+0.02	+0.02	0.12
Na I	+0.05	-0.02	-0.03	-0.03	0.07
Mg I	+0.08	-0.02	+0.03	-0.03	0.09
Al I	+0.05	+0.01	-0.01	+0.01	0.05
Si I	+0.03	+0.07	0.00	-0.03	0.08
P I	+0.03	+0.03	-0.04	-0.02	0.06
S I	-0.05	+0.05	+0.03	+0.04	0.09
K I	+0.05	+0.01	-0.03	0.00	0.06
Ca I	+0.05	-0.02	-0.02	-0.02	0.06
Sc I	+0.10	-0.03	-0.02	-0.03	0.11
Ti I	+0.09	+0.02	+0.03	+0.03	0.10
Cr I	+0.06	0.00	-0.04	-0.02	0.07
Fe I	+0.05	+0.03	+0.05	-0.02	0.08
Ni I	+0.02	+0.01	0.00	-0.02	0.03
Ce II	+0.04	+0.05	+0.01	-0.02	0.07
Nd II	+0.02	+0.04	0.00	-0.02	0.05
Yb II	+0.03	+0.08	0.00	+0.04	0.09

is derived from the uncertainty in the slope of the relation  $[\text{Fe I}/\text{H}]$  versus  $\chi$ , while the  $\xi_t$  error is estimated from the uncertainty in the slope of  $[\text{Fe I}/\text{H}]$  versus  $\log \text{EW}/\lambda$ . Surface gravity is determined iteratively by adjusting the  $\log g$  value until the difference in the average abundances of  $[\text{Fe I}/\text{H}]$  and  $[\text{Fe II}/\text{H}]$  matches the standard deviation of the mean  $[\text{Fe I}/\text{H}]$ .

These estimated uncertainties in the atmospheric parameters are subsequently propagated to assess the overall uncertainties in the chemical abundances (see Table 4). The total uncertainty in abundance, denoted as  $\sigma_{\text{atm}}$ , is computed as the square root of the sum of the squared uncertainties arising from the set of atmospheric parameters:

$$\sigma_{\text{atm}}^2 = \sigma_{T_{\text{eff}}, \log \varepsilon(X)}^2 + \sigma_{\log g, \log \varepsilon(X)}^2 + \sigma_{\Delta \log \varepsilon(\text{Fe}), \log \varepsilon(X)}^2 + \sigma_{\xi_t, \log \varepsilon(X)}^2.$$

Furthermore, Table 5 shows the variations in abundances of light chemical species (CNO). Three columns in the table demonstrate how an increment of 0.20 dex in CNO affects the abundance results since occurs an interdependence of CNO species. The uncertainty in the CNO abundances, denoted as  $\sigma_{\text{CNO}}$ , can be calculated as the square root of the sum of the squared variations in the abundances of C, N, and O:

$$\sigma_{\text{CNO}}^2 = \sigma_{\Delta \log \varepsilon(\text{C})}^2 + \sigma_{\Delta \log \varepsilon(\text{N})}^2 + \sigma_{\Delta \log \varepsilon(\text{O})}^2.$$

**Table 5.** Influence of the errors in atmospheric parameters over the abundances of CNO and isotopic ratios for NGC 2345-43. We also give the dependence of the uncertainty of CNO abundance over each light element.

$\log \varepsilon(X)$	$\Delta T_{\text{eff}}$ +80 K	$\Delta \log g$ +0.10 dex	$\Delta \log \varepsilon(\text{Fe})$ +0.07 dex	$\Delta \xi_t$ +0.17 dex	$\Delta \log \varepsilon(\text{C})$ +0.20 dex	$\Delta \log \varepsilon(\text{N})$ +0.20 dex	$\Delta \log \varepsilon(\text{O})$ +0.20 dex	$\sigma_{\text{atm}}$	$\sigma_{\text{CNO}}$
C ( $^{12}\text{C}^{16}\text{O}$ )	+0.05	+0.02	+0.05	-0.02	—	-0.06	-0.03	0.08	0.07
N ( $^{12}\text{CN}$ )	+0.05	+0.02	-0.02	-0.01	-0.34	—	+0.21	0.06	0.40
O ( $^{16}\text{OH}$ )	+0.04	-0.03	0.00	-0.03	+0.02	-0.08	—	0.06	0.08
$^{12}\text{C}/^{13}\text{C}$ ( $^{13}\text{C}^{16}\text{O}$ )	-3	-2	0	0	—	-3	-2	4	4
$^{16}\text{O}/^{17}\text{O}$ ( $^{12}\text{C}^{17}\text{O}$ )	-80	-50	+50	-50	-40	+80	—	120	90
$^{16}\text{O}/^{18}\text{O}$ ( $^{12}\text{C}^{18}\text{O}$ )	-80	-80	-40	+40	-50	+50	—	130	70

Regarding the uncertainties in the isotopic ratios, we considered the variation caused by a +0.20 dex in the abundances of the CNO species. For instance, this increment in nitrogen abundance resulted in a -0.08 dex variation in the oxygen abundance. We then propagated this variation in the oxygen abundance to calculate the corresponding variation in the isotopic ratios of  $^{16}\text{O}/^{17}\text{O}$ ,  $^{18}\text{O}$ .

### 3 DISCUSSION

Giant stars are important tracers of the chemical enrichment history of the Galaxy, as they have experienced multiple episodes of nucleosynthesis and mixing. Based on the set of abundances determined in this study, some issues can be addressed in the context of stellar evolution in the open cluster NGC 2345. Furthermore, it is crucial to undertake a comprehensive comparative abundance analysis and provide an insightful explanation for the observed differences when compared with other studies in the literature.

In this sense, H19 provided the abundances of 20 species for five stars through high-resolution OP spectra. In general, their results show relatively good agreement with the previous results obtained by Reddy, Lambert & Giridhar (2016), who reported chemical abundances of 25 elements for three stars in common with our sample (#43, #34, and #60). Also, Alonso-Santiago et al. (2019) reported good concordance with the H19's results for species analysed in both papers, except for Li, which is not investigated in this work. However, in a recent study by Tsantaki et al. (2023) about Li abundance in red giant stars of open clusters, the authors reported results that show better agreement with H19.

We will consider comparisons only between the results from NIR analysis and H19 and Carrera et al. (2022; hereafter C22; work based on OP spectra). There are 13 species in common with H19 analysed in this work, while there are 12 species in common with C22. We present the results of this study and of the last two papers in Table 3. Moreover, Table A1 provides the individual abundance results along with the respective assumed excitation potential and gf-values.

#### 3.1 Light elements: C, N, and O

CNO elements can be used as tools to understand stellar evolution, ages of stars, and stellar structures through mixing processes in red giant stars (see Randich & Magrini 2021). During the first dredge-up event, C and N experience significant changes, as a decrease in  $^{12}\text{C}$  abundance and an increase in  $^{14}\text{N}$  and  $^{13}\text{C}$  abundances. In contrast, the abundance of  $^{16}\text{O}$  is less affected by the first dredge-up. Still, its isotopic ratios undergo significant changes:  $^{16}\text{O}/^{17}\text{O}$  decreases and  $^{16}\text{O}/^{18}\text{O}$  increases, as CNO cycles produce  $^{17}\text{O}$  and destroy  $^{18}\text{O}$ . The increase of the  $^{17}\text{O}$  abundance is caused by  $^{16}\text{O}(p,\gamma)^{17}\text{F}(\beta^+)^{17}\text{O}$  reactions, until reach equilibrium through  $^{17}\text{O}(p,\alpha)^{14}\text{N}$  process.  $^{18}\text{O}$  primarily forms in the He-burning shells of massive stars via the

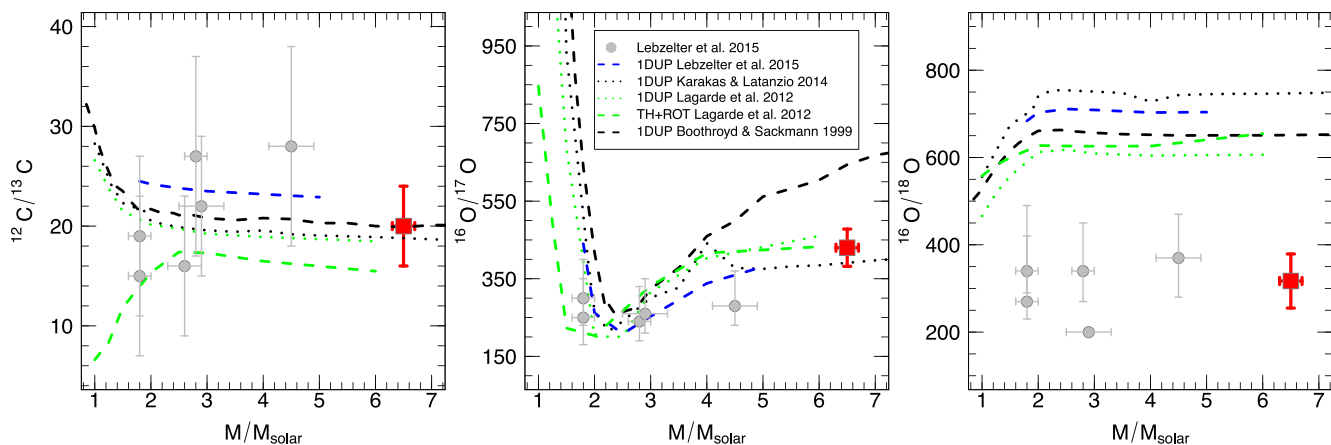


**Figure 4.** The isotopic ratios for carbon and oxygen in NGC 2345 compared with models and observations from the literature. We used three models to predict the isotope composition after the first dredge-up (1DUP): Lebzelter et al. (2015; blue dashed lines), Karakas & Lattanzio (2014; black dotted lines), Lagarde et al. (2012; standard, green dotted lines; thermohaline + rotation, green dashed lines), and Boothroyd & Sackmann (1999; black dashed lines). The grey circles represent stars analysed by Lebzelter et al. (2015). For the mean isotopic values of NGC 2345, we assumed a turn-off mass of  $6.5 M_{\odot}$  (Alonso-Santiago et al. 2019), with an uncertainty of  $0.2 M_{\odot}$ .

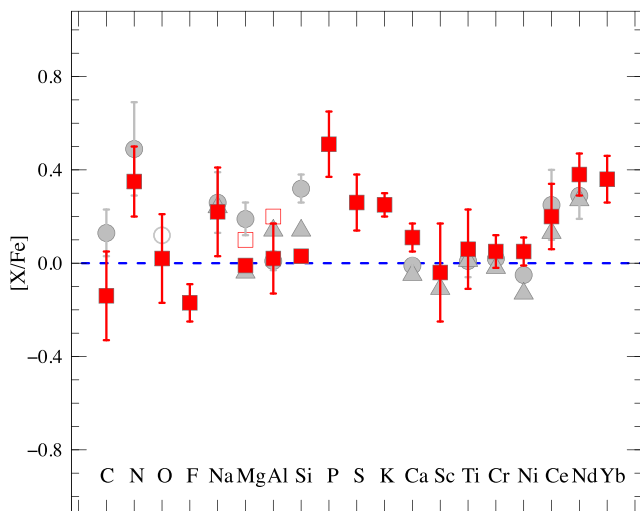


**Figure 5.** The mean elemental abundances for the NGC 2345, with results from the OP (grey circles, Holanda et al. 2019; grey triangles, Carrera et al. 2022) and NIR (red squares) spectral regions. The grey open circle represents the fixed value for [O/Fe] adopted by H19 and the red open square represents the mean magnesium and aluminum abundances under LTE conditions.

**Table 6.** Isotopic ratios for stars in our sample.

Isotopic ratio	#14	#43	#50	#60	Mean
$^{12}\text{C}/^{13}\text{C}$ (NIR)	20	24	22	15	$20 \pm 4$
$^{12}\text{C}/^{13}\text{C}$ (OP)	>24	>30	>26	>30	>27
$^{16}\text{O}/^{17}\text{O}$ (NIR)	420	400	500	400	$430 \pm 48$
$^{16}\text{O}/^{18}\text{O}$ (NIR)	300	400	320	250	$317 \pm 62$

In NIR domain  $^{13}\text{C}^{16}\text{O}$ ,  $^{12}\text{C}^{17}\text{O}$ , and  $^{12}\text{C}^{18}\text{O}$  were used.

In OP domain  $^{13}\text{C}^{14}\text{N}$  was adopted (Holanda et al. 2019).

$^{14}\text{N}(\alpha, \gamma)^{18}\text{F}(\beta^+)^{18}\text{O}$  process. In low to intermediate-mass stars, its abundance reflects the initial content and consumption rate: during hydrogen burning, it depletes through the  $^{18}\text{O}(\text{p}, \alpha)^{15}\text{N}$  reaction, and during He-burning phases, it is destroyed by the  $^{18}\text{O}(\alpha, \gamma)^{22}\text{Ne}$  process (Lebzelter et al. 2015, and references therein). In this study,

we have determined the CNO abundances of these species as well as the  $^{12}\text{C}/^{13}\text{C}$  and  $^{16}\text{O}/^{17,18}\text{O}$  isotopic ratios, providing valuable insights into the evolution of stars during the giant stage, particularly for stars with well-defined ages and masses – an advantage offered by open cluster studies.

The derivation of the  $^{16}\text{O}$  abundance can be challenging due to analytical difficulties, such as few available lines, telluric contamination, and NLTE effects. The [O I] lines at  $6300 \text{ \AA}$ , and  $6363 \text{ \AA}$ , are commonly used to determine stellar oxygen abundances, while the O I triplet at  $7771 \text{ \AA}$ , is an alternative but is significantly affected by NLTE effects. In H19, for example, the value of  $[\text{O}/\text{Fe}] = +0.12$  (typical) was fixed to obtain  $[\text{C}/\text{Fe}]$  and  $[\text{N}/\text{Fe}]$  values due to the contamination of classical lines used for that task.

The CNO results obtained from the OP and NIR analyses are in agreement when the standard deviation from the mean is considered (Table 3 and Fig. 5). However, the difference observed in C and N results demands some explanation. First, the  $^{16}\text{O}$  abundance values were determined from five regions in the *H*-band, while in the OP analysis, that was not possible, as mentioned above. The oxygen abundance is fundamental to obtaining the other abundances, C and N because there is a ‘balance’ between them. Lastly, it is essential to note that the outcomes of carbon isotopic ratios are exclusively influenced by C and N (as outlined in Table 6), given that the atmospheric parameters are the same (with minimal impact on the carbon isotopic ratio).

The carbon isotopic ratio values were determined via spectral synthesis of the  $23440 \text{ \AA}$  and  $23730 \text{ \AA}$  regions, and these values show good concordance between them but differ in comparison with the OP analysis. We identified a significant divergence in the value determined for the #60 star, which can be mainly associated with the difference in C abundance from the OP domain analysis. Also, this star presents moderate divergence in effective temperature values, which may explain the lower abundance in the sample for light chemical species such as CNO.

We present the first measurements of oxygen isotopic composition for stars in NGC 2345, which hold significant value for understanding stars with intermediate turn-off mass (see Table 6). Fig. 4 illustrates a comparison between four models (Boothroyd & Sackmann 1999; Lagarde et al. 2012; Karakas & Lattanzio 2014; Lebzelter et al. 2015)

and observational results from Lebzelter et al. (2015) for the  $^{12}\text{C}/^{13}\text{C}$  and  $^{16}\text{O}/^{17}\text{O}$ ,  $^{18}\text{O}$  ratios after the first dredge-up event. Our mean value for the  $^{12}\text{C}/^{13}\text{C}$  ratio aligns with the trends predicted by the models. Notably, for the  $^{17}\text{O}$  ratio, a good concordance is observed with the models proposed by Lagarde et al. (2012; standard prescription and thermohaline and rotation), Karakas & Lattanzio (2014), and Lebzelter et al. (2015), although with limitations for more massive stars. However, all models overestimate the  $^{16}\text{O}/^{18}\text{O}$  ratio, which is also the case for a sample of less massive stars studied by Lebzelter et al. (2015). In a prior analysis, Harris, Lambert & Smith (1988) found ratio values of  $400 \leq ^{16}\text{O}/^{18}\text{O} \leq 600$  for a sample of red giants, further contrasting with the recent models.

For low- and intermediate-mass stars, the abundance of  $^{18}\text{O}$  represents the initial value of this isotope and its destruction rate, which can occur through the process  $^{18}\text{O}(p,\alpha)^{15}\text{N}$ . Despite uncertainties in proton capture rates and mixing length, Lebzelter et al. (2015) argue that differences between the model predictions and observed ratios may be due to initial conditions. They suggest that the initial isotopic ratio might have been approximately 50 per cent of the solar value in order to bring the models and derived abundances into an agreement.

### 3.2 Fluorine

Fluorine is a very interesting element for astrophysical studies due to its diverse astrophysical sources and production channels, which include core-collapse supernovae, asymptotic giant-branch stars (AGBs), Wolf-Rayet stars, and novae (see, e.g. Ryde 2020; Womack et al. 2023). Furthermore, the abundance of fluorine has demonstrated its value as an indicator of mixing processes occurring within giant stars (e.g. Guerço et al. 2022).

In the study based on IGRINS and Phoenix high-resolution spectra, Ryde et al. (2020) determined F abundances for a sample of K giant stars, with metallicities of  $-1.1 < [\text{Fe}/\text{H}] < +0.4$ . In summary, the authors found that  $[\text{F}/\text{Fe}]$  is flat as a function of metallicity in a large interval of metallicities, but increases as the metallicity increases at supersolar metallicities regimes. Recently, Nandakumar, Ryde & Mace (2023) determined F abundances for 50 M giant stars within the solar neighbourhood using IGRINS spectra and investigated the applicability of 10 HF lines covered by IGRINS. They provided an insightful analysis of the dependence of each line on atmospheric parameters. Nandakumar and colleagues found the same fluorine abundance trends in relation to metallicity (discussed in Ryde et al. 2020) and proposed a priority sequence of line lists for accurate abundance investigations. In this study, we have presented the first-ever F abundance measurements in the literature for three stars in the open cluster NGC 2345. Star #60 was excluded from our analysis due to its significantly low fluorine abundance. Moreover, determining F abundances in ‘warm’ and non-enriched stars, as investigated in this study, presents a challenge due to the weakness of the (1-0) R9 line. This line, a key one for the HF molecule and widely adopted in the literature, is not recommended by Nandakumar, Ryde & Mace (2023), especially for the coolest and most metal-rich stars in their sample – the stars in their sample present effective temperatures ranging between 3300 and 3800 K and metallicities within  $-1.0$  and  $+0.25$  dex. The R 9 line at 23 358 Å is almost indistinguishable from the continuum for ‘warm’ stars, as demonstrated for star #43 in Fig. 3.

In Fig. 6 (top panel), we present a comparative analysis of individual fluorine-to-iron abundance ratios with the pattern delineated by Ryde et al. (2020) and Nandakumar, Ryde & Mace (2023; with re-normalization to  $\log \varepsilon(\text{F})_{\odot} = 4.56$  dex and  $\log \varepsilon(\text{Fe})_{\odot} = 7.50$  dex).

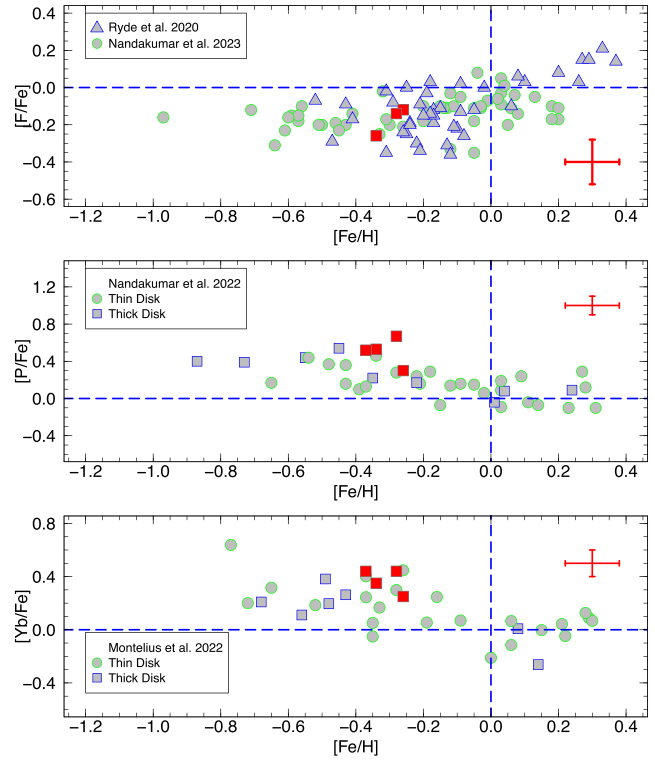


**Figure 6.** Fluorine, phosphorus and ytterbium relative to iron versus  $[\text{Fe}/\text{H}]$  for stars analysed through NIR spectra (Ryde et al. 2020; Montelius et al. 2022; Nandakumar et al. 2022; Nandakumar, Ryde & Mace 2023).

Notably, the stars of the cluster occupy a central position within the distribution and align with the established trend, indicating a relatively ‘normal’ abundance of fluorine relative to iron. The observed dispersion in the abundance trend (including #14, #43, and #50 stars), is likely attributed to its sensitivity to variations in temperature.

### 3.3 Sodium, aluminium, and phosphorus

The production of Na and Al in stars involves complex nucleosynthesis pathways. Both Na and Al can be generated through proton capture via the Ne-Na and Mg-Al chains, processes that hold particular significance in intermediate-mass stars. When compared to findings from the literature, our analysis demonstrates robust concordance between the Na abundances derived from both NIR and OP analyses (H19 and C22), as depicted in Fig. 5. In the case of Al abundances obtained under LTE conditions, an excellent alignment exists between the two spectral domain analyses across all references (LTE conditions were assumed in OP studies). To enhance the comparison, we applied NLTE corrections using the results obtained by H19, following Nordlander & Lind (2017), and found also excellent agreement with the NLTE results. Nevertheless, the ‘lower’ mean obtained after NLTE corrections aligns with the potential thin-disc stars, as shown in Fig. 7, and the pattern observed in young open clusters, as will be discussed in Section 3.7.

Fig. 7 offers a comparison between our derived results and the abundance data provided by Bensby, Feltzing & Oey (2014). This study extensively investigated the chemical composition of 714 dwarf stars in the Galactic disc, employing the thick-to-thin disc probability ratios (TD/D) for object classification (also refer to



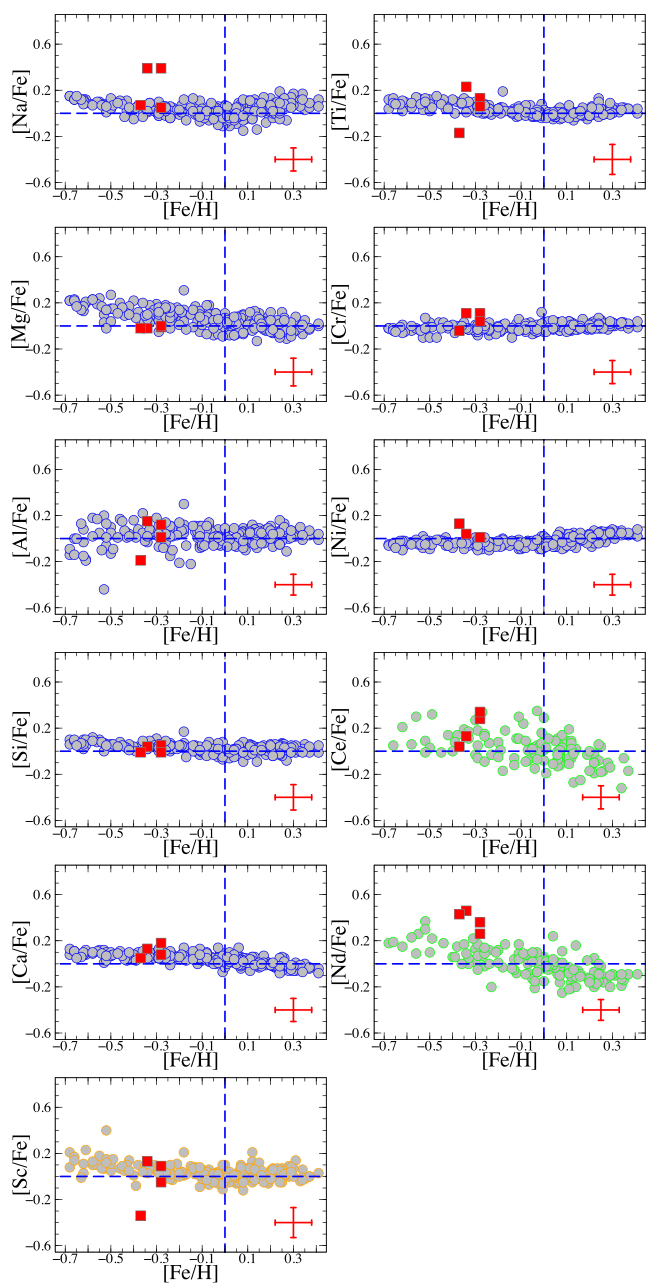


**Figure 7.** Abundance ratios  $[X/Fe]$  versus  $[Fe/H]$ . Red squares represent our sample, the circles represent the samples of dwarf stars in the thin disc analysed by Bensby, Feltzing & Oey (2014; blue), Battistini & Bensby (2015; orange), and Battistini & Bensby (2016; green), with  $\text{Age} < 7.0$  Gyr and  $\text{TD}/D < 0.5$ . The dashed lines indicate the solar values.

Bensby, Feltzing & Lundström 2003). The authors identify two predominant populations of stars: the old and  $\alpha$ -enhanced stars, primarily located within the Galactic region with  $R < 7$  kpc, and the stars with  $R > 9$  kpc that are generally younger and exhibit lower  $\alpha$ -enhancement. However, it is important to note that Bensby, Feltzing & Oey (2014) pointed out a significant bias in the kinematic criteria used to distinguish between thin- and thick-disc stars, suggesting that age might be a more reliable discriminator (determining small error bars is difficult). In this sense, we select a sub-sample with ages less than 7 Gyr, and  $\text{TD}/D < 0.5$ , as an easy decontamination of thick disc stars. In summary, this sub-sample used for comparison

can be characterized as 245 dwarf stars, with  $0.3 \leq \text{Age} < 7.0$  Gyr and  $\langle M \rangle = 1.15 M_{\odot}$ . Notably, among our sample, two stars exhibit significant enhancements in  $[Na/Fe]$  values compared to dwarf stars, a feature frequently linked with the consequences of evolutionary mixing in giant stars with masses  $\geq 2.0 M_{\odot}$  (Charbonnel & Lagarde 2010; Smiljanic 2012).

The primary site for phosphorus nucleosynthesis is core-collapse Type II supernovae (SN II; Clayton 2003). There are limited studies regarding phosphorus and its trends across various metallicities, largely due to the challenges in analysing P lines within the OP wavelength domain. However, in the IGRINS spectral coverage, it becomes feasible to employ spectral synthesis for deriving P abundance, utilizing the line at  $16482.9 \text{ \AA}$ , as employed in this study. In particular, Nandakumar et al. (2022) recently conducted a study using IGRINS spectra of 38 giant stars in the solar neighbourhood. They investigated the P abundance trend across a metallicity range of  $-1.2 < [Fe/H] < +0.4$  dex. In the middle panel of Fig. 6, we present the distribution of  $[P/Fe]$  as a function of  $[Fe/H]$ . These original abundances are normalized to the solar abundance value suggested by Grevesse, Asplund & Sauval (2007;  $\log \varepsilon(P)_{\odot} = 5.36$  dex), which diverges from the value adopted by us from Asplund et al. (2009). They derived this abundance by determining an astrophysical  $\log gf$  through reverse solar analysis of the same high-resolution spectrum (Wallace & Livingston 2003), with the discrepancy compensated by their  $gf$  value and the Afşar’s value. In Fig. 6, the stars within the open cluster exhibit  $[P/Fe]$  values that align with the trends observed in other Galactic giant stars within the same metallicity range, although a slight enrichment is discernible mainly in the case of star #43.

Nandakumar et al. (2022) discussed the predominant production site of phosphorus using a relationship between  $[P/X]$  and  $[Fe/H]$ , where X represents an odd-Z or  $\alpha$ -element. Consistent with their findings, our results also reveal phosphorus behaviour similar to  $\alpha$ -elements such as Ca and in minor amounts Si and Mg, providing further evidence for SN II as the primary origin of phosphorus.

### 3.4 Alpha elements

The ratio of  $\alpha$ -elements to iron ( $\alpha/Fe$ ) is a widely used proxy for determining the age of stars indirectly. This is because  $\alpha$ -elements, including O, Mg, Si, S, and Ca, are rapidly synthesized by SN II compared to iron, which is produced over longer time-scales by type Ia supernovae (SN Ia; Kobayashi, Karakas & Lugaro 2020). Our investigation of NGC 2345 found a mean  $[\alpha/Fe]^3$  ratio of  $+0.08 \pm 0.10$  dex, which can suggest that the gas from which these stars formed was partially enhanced by massive stars. A similar case is studied by Casamiquela et al. (2018), who analysed the young open cluster NGC 6705 and found the mean of  $[\alpha/Fe] = +0.13$  dex (in this study, we are excluding Ti abundance from the  $\alpha$ -elements set).

Our mean result for sulfur abundance appears relatively high when compared to other  $\alpha$ -elements. However, the  $\langle [S/Fe] \rangle$  value shows only a slight enrichment when compared with the sample of giant and dwarf stars analysed by Takeda et al. (2005) – the authors presented NLTE corrections for abundances derived from  $S\ 19212, 9228, 9237 \text{ \AA}$  lines, as well as verify the validity of LTE abundances from  $8683$  to  $8694 \text{ \AA}$  lines. It is worth noting that the authors used a solar value of  $\log \varepsilon(S)_{\odot} = 7.21$  dex, and a simple re-normalization might be sufficient to achieve a good agreement with the results obtained for the stars in NGC 2345. Also, regarding

$$^3[\alpha/Fe] = \frac{1}{3}([\text{O}/\text{Fe}] + [\text{Mg}/\text{Fe}] + [\text{Si}/\text{Fe}] + [\text{S}/\text{Fe}] + [\text{Ca}/\text{Fe}])$$

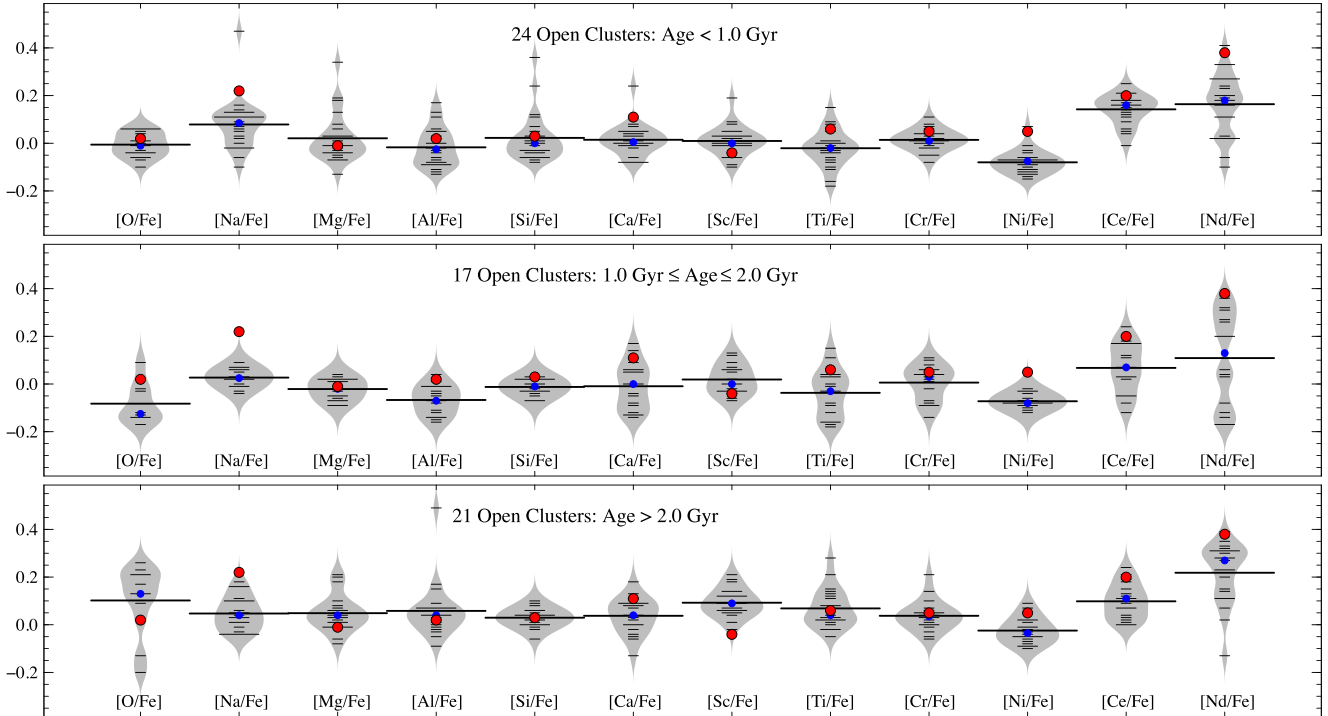


**Figure 8.** Beanplots of abundances relative to iron for open clusters analysed by Magrini et al. (2023; OP spectra). The individual observations are shown as short lines, the means as thick lines, and the median is denoted by the blue circles. The mean abundance results for the cluster NGC 2345 are represented by the red circles. In this comparison, the clusters are organized in subsets by age: Age < 1.0 Gyr,  $1.0 \leq \text{Age} \leq 2.0$  Gyr, and Age > 2.0 Gyr.

NIR analyses, the lines at  $\lambda$  22507, 22519, 22526, and 22563 Å do not have available NLTE corrections in the literature. However, when we compare our LTE abundances to the NLTE results obtained by Takeda et al. (2005) while taking into account a re-normalization, we suggest that NLTE effects have a relatively minor impact on these lines in the *K*-band. In a recent study, Takeda et al. (2016) examined a substantial sample of 239 field GK giants and calculated NLTE corrections for S I abundances. They emphasized the reliability of the S I 6757 Å line as an indicator of sulfur abundance and found a typical difference of less than 0.10 dex between NLTE and LTE conditions. When we compare our  $[\text{S}/\text{Fe}]$  result with the  $[\text{Fe}/\text{H}]$  vs.  $[\text{S}/\text{Fe}]$  distribution depicted in Takeda et al.’s Fig. 8, our findings indicate only a slight enrichment, suggesting a minimal impact of NLTE effects.

Additionally, our study presents the first abundance determination of potassium (an odd-*Z* element) for stars in this open cluster. However, our results can be masked by NLTE effects. Unfortunately, the study of the NLTE effects on transition adopted by us has not been investigated. But, comparing our results with red giant stars analysed by Takeda (2020; Fig. 7 in that paper), we note a minimal overabundance in our results relative to other giants of similar metallicity (Takeda used OP high-resolution spectra). This shy difference agrees with Afşar et al. (2018), who suggested that K I 15163 Å line may provide abundances less affected by NLTE. Despite a small impact of NLTE correction in K abundance values, our measured mean value also agrees with  $\alpha$ -elements. Kobayashi et al. (2011) has previously demonstrated that the abundance of K can be increased by the neutrino process in SN II, which is consistent with our finding of a slight enrichment in K abundance in the sample.

The most significant differences between the abundances derived from the two domains are observed in the Mg, Si, and Ca abundances, with mean discrepancies of  $\langle \Delta \text{Mg} \rangle = +0.20$  dex and  $\langle \Delta \text{Si} \rangle = +0.29$  dex. A minor difference is observed for LTE

magnesium abundances ( $\langle \Delta \text{Mg} \rangle = +0.09$  dex). Additionally, it can be inferred that the results for Mg abundance derived from OP analysis tend to be overestimated. For instance, this overestimation may be partially attributed to the impact of departures from LTE on two critical spectral lines: those at 8717 and 8736 Å. These lines exhibit a displacement of approximately  $-0.1$  dex for the stars in our sample, as indicated by the models developed by Osorio & Barklem (2016).

The NIR results also demonstrate a good alignment with the Mg and Si abundance patterns observed in thin-disc stars, as shown in Fig. 7. Section 3.7 will provide a comprehensive illustration of the  $[\text{Si}/\text{Fe}]$  and  $[\text{Ca}/\text{Fe}]$  behaviour in additional young open clusters studied in the literature, further solidifying the reliability of the NIR abundance results.

### 3.5 Iron-peak elements

Iron-peak elements such as Sc, Ti, Fe, Ni, and Cr are, in part, products of SN II. However, it is worth noting that low-mass stars in binary systems also contribute to the production of these chemical species through explosive nucleosynthesis during SN Ia. This last process implies a longer time-scale for the production of iron-peak elements.

In a comprehensive study, Battistini & Bensby (2015) analysed the origin and evolution of iron-peak elements such as Sc, V, Mn, and Co for different Galactic populations. Their sample matches that used in Bensby, Feltzing & Oey (2014), prompting us to apply the same filters to isolate probable thin-disc stars for comparison. Fig. 7 displays the abundances of iron-peak elements derived from NIR analysis, which align with the results for dwarf stars in the same metallicity range. To investigate distinctions between Galactic disc populations, Battistini & Bensby (2015) employed medians to identify different trends for the sample of dwarf stars with wide intervals of ages. For

Sc abundances, they distinguished two different groups, with the one associated with the thin disc (comprising younger stars) displaying a less steep increase in [Sc/Fe], consistent with the behaviour of the three stars in our sample. The authors also suggest that both Sc and Ti share the same production site (where Ti was considered an  $\alpha$ -element).

The ratio abundance values of [Ti/Fe], [Cr/Fe], and [Ni/Fe] derived in our NIR analysis are in good concordance with the results obtained from the OP analysis by H19, all of which presented differences of less than 0.10 dex. Relative to the results obtained by C22, there is an agreement in the mean difference of 0.10 dex for [Sc/Fe], [Ti/Fe], [Cr/Fe], and [Ni/Fe], but the reader should be aware of this comparison because the authors analysed only two stars in common with us (#43 and #60).

### 3.6 Heavy elements: Ce, Nd, and Yb

The slow and rapid neutron capture processes (s- and r-process) produce isotopes heavier than the iron. Their astrophysical sources are currently associated with low-mass AGB stars and explosive nucleosynthesis by massive stars, respectively (e.g. Gallino et al. 1998; Busso, Gallino & Wasserburg 1999; Thielemann et al. 2011).

In this study, we analysed three heavy chemical species. The cerium and neodymium abundances present at the epoch of the solar system formation are predominantly attributed to the s-process (83 per cent and 57 per cent, respectively, Bisterzo et al. 2014), while the ytterbium abundance is mainly associated with the r-process (60 per cent, Bisterzo et al. 2014) and is relatively little explored in the literature. To check the correspondence between the two analyses (NIR vs. OP), the Ce and Nd abundances determined via NIR analysis are in excellent agreement with OP results, as shown in Fig. 5 – for H19’s values:  $\langle \Delta \text{Ce} \rangle = -0.05$  dex and  $\langle \Delta \text{Nd} \rangle = +0.08$  dex; and for C22’s results:  $\langle \Delta \text{Ce} \rangle = +0.07$  dex and  $\langle \Delta \text{Nd} \rangle = -0.11$  dex).

The abundance of s-process elements in stars of open clusters can be an important clue to understanding how the posterior stellar generation could inherit heavy elements. In this context, we confirm the finding by other authors about this cluster, as well as other open clusters with ages less than a few hundred Myr, that present slight enrichment in s-process elements (Alonso-Santiago et al. 2019, 2020; Holanda et al. 2021, 2022, and many others). For a comprehensive comparison, we compare our Ce and Nd abundance results with those obtained by Battistini & Bensby (2016) for a sample of dwarf stars in the solar neighbourhood, which constitutes a subset of the stars investigated by Bensby, Feltzing & Oey (2014). This comparison reinforces the hypothesis of a slight enhancement in s-process elements, as illustrated in Fig. 7. We applied the same selection criteria employed for the sample analysed by Bensby, Feltzing & Oey (2014) to identify likely thin-disc stars, resulting in a subset of 146 objects with  $0.4 \leq \text{Age} < 7.0$  Gyr, and  $\langle M \rangle = 1.12 M_{\odot}$ . Among these, stars #50 and #60 exhibit [Ce/Fe] values that closely align with the central distribution of thin disc dwarf stars. Nevertheless, when considering all four stars, the overall mean value still suggests a slight enrichment. This observation is explored further in Section 3.7, where we compare our means with different sets of open clusters categorized by varying age ranges.

D’Orazi et al. (2009) observed a significant increasing trend of barium abundance (one of the best representative of s-process elements, 85 per cent; Bisterzo et al. 2014), as a function of the cluster age. Later, Maiorca et al. (2011, 2012) confirmed their findings and investigated other s-process elements such as Y, Zr, La, and Ce. There is no definitive explanation for this odd trend, but a possible clue is associated with enhanced production of neutron-

capture nuclei by low-mass AGB stars (see a revision in D’Orazi et al. 2022). Also, we do not identify any enrichment in fluorine (Section 3.2 and Fig. 6), an element enhanced in s-process-rich AGB stars (Abia et al. 2010). In this context, in a recent study, Ryde et al. (2020) studied cool giants and found a flat distribution of the [F/Ce] ratio for  $-0.6 < [\text{Fe}/\text{H}] < 0.0$  dex. Interestingly, they also observed no fluorine enhancement in two metal-poor stars with s-process element enrichment ( $[\text{Fe}/\text{H}] < -0.8$  dex). This indicates a significant contribution from AGB stars within the  $-0.6 < [\text{Fe}/\text{H}] < 0.0$  dex range. However, our findings deviate from this pattern, as we notice only Ce and Nd enrichment and no significant (or notable) increase in fluorine abundance. To comprehend potential scenarios involving simultaneous enrichment of s-process elements and fluorine with decreasing age, an extensive investigation of fluorine abundance within young open clusters is imperative.

The measurement of ytterbium, an r-process element, has been limited to a few stars to date. In a recent study by Montelius et al. (2022), IGRINS spectra were used to analyse ytterbium abundance in giants across a metallicity range of  $-1.2 < [\text{Fe}/\text{H}] < +0.3$  dex. As shown in the bottom panel of Fig. 6, a trend in [Yb/Fe] values is evident, similar to the trend observed in europium abundance, a ‘pure’ r-process element (95 per cent; Bisterzo et al. 2014; Montelius et al. 2022). This trend aligns with the findings of Forsberg et al. (2019), who made a differential comparison of heavy element abundances in the Galactic bulge and local disc, focusing on Zr, La, Ce, and Eu. Their study indicated a dominance of the r-process in the early n-capture production for both the disc and the bulge. Regarding [Eu/Fe], they observed a clear decreasing trend with increasing metallicities in both regions, a trend also noticeable in Fig. 6 for [Yb/Fe]. This pattern bears resemblance to the typical trend observed in  $\alpha$ -elements, suggesting a similar production rate.

The Yb abundance for this cluster has been determined for the first time, and our results align with the trend observed by Montelius et al., as well as with the findings of Böcek Topcu et al. (2019, 2020), who conducted studies on the open clusters NGC 752 and NGC 6940. However, it is noteworthy that in Fig. 5 of Montelius and colleagues, a scatter is evident at lower metallicities, which could be linked to inhomogeneities in the Galactic interstellar medium at such low metallicity levels. Notably, events like mergers of neutron stars and magneto-rotational-supernovae (Kobayashi, Karakas & Lugaro 2020) have the potential to create isolated stellar groups with either high or low r-process abundances. Nevertheless, in the higher metallicity regime, a more uniform and consistent enrichment pattern appears to be prevalent (Montelius et al. 2022, and references therein).

### 3.7 Chemical clocks

One significant facet explored within the spectroscopic surveys is the concept of chemical clocks, aimed at establishing correlations between the ratios of chemical abundances and the evolutionary parameters of stars and clusters, which include age and Galactocentric distance. As the number of studies dedicated to this topic has grown, predominantly utilizing OP spectra, several correlations have been established. In this context, the consistency of abundances of s-process and  $\alpha$ -elements has been observed over a broad range of ages for open clusters (e.g. Katime Santrich et al. 2022; Viscasillas Vázquez et al. 2022).

Recently, Sales-Silva et al. (2022) conducted a study investigating the correlation between Ce abundance ratios and age within a sample of 40 open clusters. Their analysis involved abundance data obtained from NIR spectra collected through the APOGEE survey (Wilson

**Table 7.** Mean abundances of NGC 2345 and the mean and median values from clusters analysed by Magrini et al. (2023), categorized by age range. The last line corresponds to the mean absolute deviation concerning the differences from the mean ( $\text{Diff}_{\text{Mean}}$ ) and median ( $\text{Diff}_{\text{Median}}$ ).

Ratio	NGC 2345	Age < 1.0 Gyr				1.0 ≤ Age ≤ 2.0 Gyr				Age > 2.0 Gyr			
		Mean	Median	$\text{Diff}_{\text{Mean}}$	$\text{Diff}_{\text{Median}}$	Mean	Median	$\text{Diff}_{\text{Mean}}$	$\text{Diff}_{\text{Median}}$	Mean	Median	$\text{Diff}_{\text{Mean}}$	$\text{Diff}_{\text{Median}}$
[O/Fe]	+0.02	−0.01	−0.01	+0.03	+0.03	−0.08	−0.12	+0.10	+0.14	+0.10	+0.13	−0.08	−0.11
[Na/Fe]	+0.22	+0.08	+0.09	+0.14	+0.13	+0.03	+0.03	+0.19	+0.19	+0.05	+0.04	+0.17	+0.18
[Mg/Fe]	−0.01	+0.02	−0.01	−0.03	0.00	−0.02	−0.02	+0.01	+0.01	+0.05	+0.04	−0.06	−0.05
[Al/Fe]	+0.02	−0.02	−0.02	+0.04	+0.04	−0.07	−0.07	+0.09	+0.09	+0.06	+0.04	−0.04	−0.02
[Si/Fe]	+0.03	+0.02	0.00	+0.01	+0.03	−0.01	−0.01	+0.04	+0.04	+0.03	+0.03	0.00	0.00
[Ca/Fe]	+0.11	+0.01	+0.01	+0.10	+0.10	−0.01	0.00	+0.12	+0.11	+0.04	+0.04	+0.07	+0.07
[Sc/Fe]	−0.04	−0.01	0.00	+0.03	−0.04	+0.02	0.00	−0.06	−0.04	+0.09	+0.09	−0.13	−0.13
[Ti/Fe]	+0.06	−0.02	−0.02	+0.08	+0.08	−0.04	−0.03	+0.10	+0.09	+0.07	+0.04	−0.01	+0.02
[Cr/Fe]	+0.05	+0.01	+0.01	+0.04	+0.04	+0.01	+0.03	+0.04	+0.02	+0.04	+0.04	+0.01	+0.01
[Ni/Fe]	+0.05	−0.08	−0.07	+0.13	+0.12	−0.07	−0.08	+0.12	+0.13	−0.02	−0.03	+0.07	+0.08
[Ce/Fe]	+0.20	+0.14	+0.16	+0.06	+0.04	+0.07	+0.07	+0.13	+0.13	+0.10	+0.10	+0.10	+0.10
[Nd/Fe]	+0.38	+0.16	+0.18	+0.22	+0.20	+0.11	+0.13	+0.27	+0.25	+0.22	+0.27	+0.16	+0.11
MAD				0.05	0.06			0.07	0.07			0.10	0.10

et al. 2019). The authors categorized their sample into subgroups and identified a consistent trend of decreasing Ce abundance with increasing age. In this study, we considered two Ce lines from the set analysed by Sales-Silva et al. (2022; 16376 Å and 16595 Å, and same  $g_f$ -values) and adopted the linear fit for the trend they observed, specifically for Age < 1.0 Gyr, and  $R_{\text{GC}} = 10.22$  kpc: we take into account  $d = 2.5 \pm 0.2$  kpc by Alonso-Santiago et al. (2019) and solar Galactocentric distance of  $R_{\odot} = 8.34 \pm 0.16$  kpc by Reid et al. (2014). The relationship proposed by Sales-Silva et al. (2022) takes the following form:  $[\text{Ce}/\text{Fe}] = 0.018 \times R_{\text{GC}} + 0.116$ .

The results obtained from both OP and NIR spectral analyses are aligned with the trend, indicating a  $[\text{Ce}/\text{Fe}]$  value of +0.30 dex for the cluster’s  $R_{\text{GC}}$ . Most recently, Magrini et al. (2023) utilized a sample of 62 open clusters within the framework of the *Gaia*-ESO survey (Gilmore et al. 2012, 2022) to trace Galactic radial abundance and its temporal evolution, based on high-resolution OP spectra. In Fig. 8, we compare the mean abundances relative to iron for NGC 2345 (red circle) and classify the sample analysed by Magrini et al. (2023) into three subsets: Age < 1.0 Gyr,  $1.0 \leq \text{Age} \leq 2.0$  Gyr, and Age > 2.0 Gyr. The grey area of the beanplot reflects the densities of individual open cluster abundances, represented by short lines, and the mean for each abundance relative to iron is depicted by a thick line. Supplementary information is conveyed through the median abundance, indicated by a blue circle (additional information about the R package beanplot can be found in Kampstra 2008). Among the younger subset, we find that the mean values are quite similar to those of NGC 2345, and the most notable discrepancies are observed in  $[\text{Na}/\text{Fe}]$ ,  $[\text{Ni}/\text{Fe}]$ , and  $[\text{Nd}/\text{Fe}]$  ratios. Interestingly, NGC 2345 does not claim the title of the most enriched cluster for these chemical species in this comparative abundance analysis. Also, it is important to note that the dataset from Magrini and colleagues includes just four clusters with ages below 200 Myr. This limited number of young clusters restricts the scope of comparison, especially regarding the enrichment of s-process elements, as younger clusters typically exhibit more pronounced mean enrichment. Additionally, the younger open clusters in this sample tend to be situated at Galactocentric distances of less than 9 kpc, which could account for discrepancies in the abundance ratios.

In Table 7, we present the mean abundance values for NGC 2345, as well as the mean and median values from clusters analysed by Magrini et al. (2023), categorized by age. We also included the differences between the mean values of NGC 2345 and the mean ( $\text{Diff}_{\text{Mean}}$ ) and median ( $\text{Diff}_{\text{Median}}$ ) values of the clusters from the

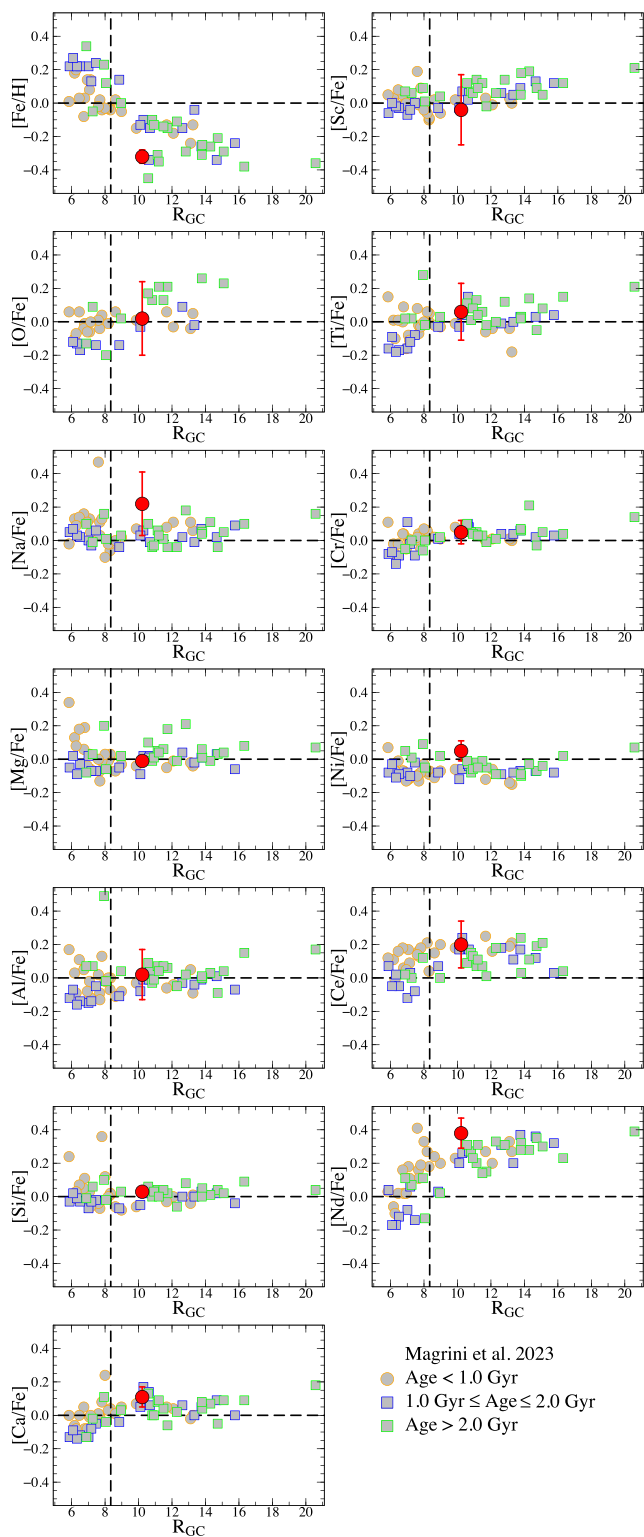
literature. The last line corresponds to the mean absolute deviation (MAD) results related to the differences  $\text{Diff}_{\text{Mean}}$  and  $\text{Diff}_{\text{Median}}$ . Consequently, we observe that the derived abundance set for NGC 2345 exhibits a better agreement with the median for young open clusters analysed by Magrini et al. (2023), even considering the mentioned limitations.

Fig. 9 presents the Galactocentric distances plotted against the relative abundances for the open cluster sample analysed by Magrini et al. (2023), employing the same age classification. A notable gap is evident within the set of younger clusters, particularly in the vicinity of NGC 2345, where a majority of the clusters are concentrated at distances less than 9.0 kpc. Nevertheless, when examining the outcomes related to the Melotte 71 cluster (the grey circle at  $R_{\text{GC}} = 9.87$  kpc), it becomes evident that there is a significant agreement in the derived abundances for NGC 2345, although differing in terms of the  $[\text{Fe}/\text{H}]$  values. Importantly, this comparison does not rely on the mean values for all clusters, as presented in Fig. 8, since ratios such as  $[\text{Na}/\text{Fe}]$ ,  $[\text{Ni}/\text{Fe}]$ , and  $[\text{Nd}/\text{Fe}]$  align with Melotte 71’s values when accounting for standard deviations from the mean. The inclusion of more young open clusters with  $R_{\text{GC}} = 9\text{--}11$  kpc is fundamental for constructing a robust comparison.

On the contrary, when comparing with the cluster set with ages between 1.0 and 2.0 Gyr, we obtain more favourable outcomes. This set includes four open clusters (NGC 2355, Collinder 110, NGC 2506, and NGC 2420) with Galactocentric distances similar to that of NGC 2345. Notably, NGC 2506 exhibits very close values for iron abundance and Galactocentric distance (−0.34 and 10.62 kpc, respectively). Finally, when we compare the results determined for stars in NGC 2345 with the older open clusters (Age > 2.0 Gyr), we find a good number of clusters with similar distances. The apparent better agreement with the older cluster could be attributed to the scarcity of young clusters in the NGC 2345’s region. However, the NGC 2345 cluster stands out due to its low metallicity, which is very similar to that of a group of older clusters. A possible explanation for this is proposed by Baratella et al. (2020), who studied the impact of the hot active chromosphere in dwarf stars and argued that there might be limitations associated with the conventional spectral analysis based only on iron lines when deriving atmospheric parameters.

#### 4 SUMMARY

In this study, we determined the abundances of 20 chemical species in stars of the NGC 2345 open cluster, including results of five species



**Figure 9.** Galactocentric distances versus relative abundances for open clusters analysed by Magrini et al. (2023). The dashed lines indicate the solar values.

reported for the first time (F, P, S, K, and Yb). For the majority of the elements studied, we confirmed the abundance values determined via OP spectra analysis based on a previous study done by Holanda et al. (2019) and in another recent article from the literature (Carrera et al. 2022). The  $^{16}\text{O}$  abundance was derived from the OH band in different regions of the spectra, which made it possible to determine  $^{12}\text{C}$  and  $^{14}\text{N}$  abundances via an interactive method, justifying the discrepancies relative to our OP study for the same stars, since the  $^{16}\text{O}$  value was necessarily fixed due to telluric contamination in the line at 6300 Å, which is classically used for analysis in the OP domain.

For the elements Na, Al, Ti, Cr, Fe, Ni, Ce, and Nd, their abundance ratios are in relatively good agreement with those previously derived from OP spectra (differences up to 0.1 dex), which is not surprising and shows the reliability of the *gf*-values recommended by Afşar et al. (2018) and others for these atomic lines in the NIR region. The use of IGRINS makes it possible to increase the number of studies providing reliable abundance data from high-resolution NIR spectra, aiming to complement the investigations introduced via OP analysis works. Moreover, obscured open clusters (or in dense regions), recently discovered, may become studied thanks to possibilities such as those for *H*- and *K*-bands. Indeed, a combination of different spectral domains is promising and may be helpful to better describe/characterize open problems in stellar astrophysics, as well as the nature of different classes of chemically peculiar stars, such as Ba stars, Li-rich giant stars, and weak *G* band stars (Adamczak & Lambert 2013; Holanda, Drake & Pereira 2023), in the sense that additional abundances, such as  $^{19}\text{F}$  and isotopes as  $^{17}\text{O}$  and  $^{18}\text{O}$ , can be addressed.

The results for  $^{12}\text{C}/^{13}\text{C}$  and  $^{16}\text{O}/^{17}\text{O}$  ratios are consistent with the values predicted by the models of Boothroyd & Sackmann (1999), Lagarde et al. (2012), Karakas & Lattanzio (2014), and Lebzelter et al. (2015). However, all the models overestimate the  $^{16}\text{O}/^{18}\text{O}$  ratio, which is also true for a sample of less-massive stars from the literature. The differences between the model predictions and observed ratios may be due to initial conditions in the models. Lebzelter et al. (2015) suggest that the initial isotopic ratio might have been  $\approx 50$  per cent of the solar value to bring the models and derived abundances into an agreement. Our measurements, combined with precise mass determinations for open cluster studies, can provide minor uncertainties and a better valuation for the models.

Finally, regarding the Galactic Ce abundance for open clusters as a function of the Galactocentric distance, metallicity, and age, we found good agreement with the trends observed by Sales-Silva et al. (2022). The  $\langle [\text{Ce}/\text{Fe}] \rangle$  and  $\langle [\text{Nd}/\text{Fe}] \rangle$  values obtained in this paper through NIR spectra confirm the observed slight enhancement in s-process element abundance among young open clusters, as extensively documented in existing literature. Furthermore, when conducting a comparison with the cluster sample analysed by Magrini et al. (2023), it becomes evident that a limited number of young clusters are positioned within the Galactocentric distances of 9–11 kpc. Despite these limitations, we observe a relatively favourable agreement with the young open clusters studied by Magrini and colleagues. This agreement is underscored by the mean absolute deviation calculated for the abundance ratios of 12 elements relative to iron. However, the low metallicity for the cluster NGC 2345 is only observable in older clusters ( $>1.0$  Gyr) at similar Galactocentric distances.

## ACKNOWLEDGEMENTS

We would like to thank the referee for constructive comments and suggestions that helped in improving the manuscript. We also express our appreciation to Thomas Nordlander and Yeisson Osorio for their generous assistance. This work has been developed under a fellowship of the PCI Program of the Ministry of Science, Technology, and Innovation, financed by the Brazilian National Council of Research – CNPq. NAD acknowledges Fundação de Amparo à Pesquisa do Estado do Rio de Janeiro – FAPERJ, Rio de Janeiro, Brazil, for grant E-26/203.847/2022. SD acknowledges the support from CNPq (PQ 306859/2022-0). MPR acknowledges a fellowship (300922/2023-0) of the PCI Program – MCTI and CNPq. We express our appreciation to Thomas Nordlander and Yeisson Osorio for their generous assistance. We are also thankful for the invaluable assistance provided by IGRINS support astronomers Gregory Mace and Venu Kalari.

This work used the Immersion Grating Infrared Spectrometer (IGRINS) that was developed under a collaboration between the University of Texas at Austin and the Korea Astronomy and Space Science Institute (KASI) with the financial support of the Mt. Cuba Astronomical Foundation, of the US National Science Foundation under grants AST-1229522 and AST-1702267, McDonald Observatory of the University of Texas at Austin, of the Korean GMT Project of KASI, and Gemini Observatory.

*Software:* IRAF (Tody 1986), MOOG (Snedden et al. 2012), LINE-MAKE (Placco et al. 2021), R, and RSTUDIO (RStudio Team 2020; R Core Team 2021).

## DATA AVAILABILITY

Data are available on request. The data underlying this article will be shared on reasonable request to the corresponding author.

## REFERENCES

- Abia C. et al., 2010, *ApJ*, 715, L94  
 Adamczak J., Lambert D. L., 2013, *ApJ*, 765, 155  
 Afşar M. et al., 2016, *ApJ*, 819, 103  
 Afşar M. et al., 2018, *ApJ*, 865, 44  
 Alonso-Santiago J., Negueruela I., Marco A., Taberner H. M., González-Fernández C., Castro N., 2019, *A&A*, 631, A124  
 Alonso-Santiago J., Negueruela I., Marco A., Taberner H. M., Castro N., 2020, *A&A*, 644, A136  
 Alonso A., Arribas S., Martínez-Roger C., 1999, *A&AS*, 140, 261  
 Asplund M., Grevesse N., Sauval A. J., Scott P., 2009, *ARA&A*, 47, 481  
 Baratella M. et al., 2020, *A&A*, 634, A34  
 Battistini C., Bensby T., 2015, *A&A*, 577, A9  
 Battistini C., Bensby T., 2016, *A&A*, 586, A49  
 Bensby T., Feltzing S., Lundström I., 2003, *A&A*, 410, 527  
 Bensby T., Feltzing S., Oey M. S., 2014, *A&A*, 562, A71  
 Bisterzo S., Travaglio C., Gallino R., Wiescher M., Käppeler F., 2014, *ApJ*, 787, 10  
 Böcek Topcu G. et al., 2019, *MNRAS*, 485, 4625  
 Böcek Topcu G. et al., 2020, *MNRAS*, 491, 544  
 Boothroyd A. I., Sackmann I. J., 1999, *ApJ*, 510, 232  
 Brooke J. S., Bernath P. F., Western C. M., Sneden C., Afşar M., Li G., Gordon I. E., 2016, *JQSRT*, 168, 142  
 Busso M., Gallino R., Wasserburg G. J., 1999, *ARA&A*, 37, 239  
 Cantat-Gaudin T. et al., 2020, *A&A*, 640, A1  
 Carrera R. et al., 2022, *A&A*, 663, A148  
 Casamiquela L. et al., 2018, *A&A*, 610, A66  
 Charbonnel C., Lagarde N., 2010, *A&A*, 522, A10  
 Civiš S., Ferus M., Chernov V. E., Zanozina E. M., 2013, *A&A*, 554, A24  
 Clayton D., 2003, *Handbook of Isotopes in the Cosmos*. Cambridge University Press, Cambridge  
 Cox A. N., 2000, *Allen's astrophysical quantities*. 4th ed., AIP Press, New York  
 Cunha K. et al., 2017, *ApJ*, 844, 145  
 Cutri R. M. et al., 2003, *VizieR Online Data Catalog*, p. II/246  
 D'Orazi V., Magrini L., Randich S., Galli D., Busso M., Sestito P., 2009, *ApJ*, 693, L31  
 D'Orazi V., Baratella M., Lugaro M., Magrini L., Pignatari M., 2022, *Universe*, 8, 110  
 Forsberg R., Jönsson H., Ryde N., Matteucci F., 2019, *A&A*, 631, A113  
 Friel E. D., 1995, *ARA&A*, 33, 381  
 Fukue K. et al., 2015, *ApJ*, 812, 64  
 Gallino R., Arlandini C., Busso M., Lugaro M., Travaglio C., Straniero O., Chieffi A., Limongi M., 1998, *ApJ*, 497, 388  
 Gilmore G. et al., 2012, *The Messenger*, 147, 25  
 Gilmore G. et al., 2022, *A&A*, 666, A120  
 Goorvitch D., 1994, *ApJS*, 95, 535  
 Grevesse N., Asplund M., Sauval A. J., 2007, *Space Sci. Rev.*, 130, 105  
 Guêrço R. et al., 2022, *MNRAS*, 516, 2801  
 Harris M. J., Lambert D. L., Smith V. V., 1988, *ApJ*, 325, 768  
 Hasselquist S. et al., 2016, *ApJ*, 833, 81  
 Holanda N., Pereira C. B., Drake N. A., 2019, *MNRAS*, 482, 5275  
 Holanda N., Drake N. A., Pereira C. B., 2020a, *MNRAS*  
 Holanda N., Drake N. A., Pereira C. B., 2020b, *AJ*, 159, 9  
 Holanda N., Drake N. A., Corradi W. J. B., Ferreira F. A., Maia F., Magrini L., da Silva J. R. P., Pereira C. B., 2021, *MNRAS*, 508, 5786  
 Holanda N., Ramos A. A., Peña Suárez V. J., Martínez C. F., Pereira C. B., 2022, *MNRAS*, 516, 4484  
 Holanda N., Drake N. A., Pereira C. B., 2023, *MNRAS*, 518, 4038  
 Jönsson H. et al., 2014, *A&A*, 564, A122  
 Kampstra P., 2008, *J. Stat. Softw.*, 28, 1  
 Karakas A. I., Lattanzio J. C., 2014, *Publ. Astron. Soc. Aust.*, 31, e030  
 Katime Santrich O. J., Kerber L., Abuchaim Y., Gonçalves G., 2022, *MNRAS*, 514, 4816  
 Kobayashi C., Izutani N., Karakas A. I., Yoshida T., Yong D., Umeda H., 2011, *ApJ*, 739, L57  
 Kobayashi C., Karakas A. I., Lugaro M., 2020, *ApJ*, 900, 179  
 Kramida A., Ralchenko Y., Reader J. et al., 2014, URL <https://physics.nist.gov/asd>  
 Krumholz M. R., McKee C. F., Bland-Hawthorn J., 2019, *ARA&A*, 57, 227  
 Kurucz R. L., 2011, *Can. J. Phys.*, 89, 417  
 Lada C. J., Lada E. A., 2003, *ARA&A*, 41, 57  
 Lagarde N., Decressin T., Charbonnel C., Eggenberger P., Ekström S., Palacios A., 2012, *A&A*, 543, A108  
 Lebzelter T., Straniero O., Hinkle K. H., Nowotny W., Aringer B., 2015, *A&A*, 578, A33  
 Magrini L. et al., 2023, *A&A*, 669, A119  
 Maiorca E., Randich S., Busso M., Magrini L., Palmerini S., 2011, *ApJ*, 736, 120  
 Maiorca E., Magrini L., Busso M., Randich S., Palmerini S., Trippella O., 2012, *ApJ*, 747, 53  
 Martínez C. F., Holanda N., Pereira C. B., Drake N. A., 2020, *MNRAS*, 494, 1470  
 Mermilliod J. C., Mayor M., Udry S., 2008, *A&A*, 485, 303  
 Montelius M. et al., 2022, *A&A*, 665, A135  
 Nandakumar G., Ryde N., Montelius M., Thorsbro B., Jönsson H., Mace G., 2022, *A&A*, 668, A88  
 Nandakumar G., Ryde N., Mace G., 2023, *A&A*, 676, 79  
 Netopil M., Paunzen E., Heiter U., Soubiran C., 2016, *A&A*, 585, A150  
 Nordlander T., Lind K., 2017, *A&A*, 607, A75  
 Osorio Y., Barklem P. S., 2016, *A&A*, 586, A120  
 Osorio Y., Barklem P. S., Lind K., Belyaev A. K., Spielfiedel A., Guitou M., Feautrier N., 2015, *A&A*, 579, A53  
 Park S. et al., 2018, *ApJS*, 238, 29  
 Pehlivan A., Nilsson H., Hartman H., 2015, *A&A*, 582, A98  
 Pereira C. B., Holanda N., Drake N. A., Roig F., 2019, *AJ*, 157, 70  
 Placco V. M., Sneden C., Roederer I. U., Lawler J. E., Den Hartog E. A., Hejazi N., Maas Z., Bernath P., 2021, *Res. Notes Am. Astron. Soc.*, 5, 92  
 Core R., 2021, *R: A Language and Environment for Statistical Computing*. R Foundation for Statistical Computing, Vienna, Austria

- RStudio Team, 2020, RStudio: Integrated Development Environment for R. RStudio, PBC., Boston, MA
- Randich S., Magrini L., 2021, *Front. Astron. Space Sci.*, 8, 6
- Reddy A. B. S., Lambert D. L., Giridhar S., 2016, *MNRAS*, 463, 4366
- Reid M. J. et al., 2014, *ApJ*, 783, 130
- Ryde N., 2020, *J. Astrophys. Astron.*, 41, 34
- Ryde N. et al., 2020, *ApJ*, 893, 37
- Sales-Silva J. V. et al., 2022, *ApJ*, 926, 154
- Skiff B. A., 2014, VizieR Online Data Catalog, p. B/mk
- Smiljanic R., 2012, *MNRAS*, 422, 1562
- Smith V. V. et al., 2013, *ApJ*, 765, 16
- Snedden C. A., 1973, PhD thesis, The University of Texas at Austin
- Snedden C., Bean J., Ivans I., Lucatello S., Sobek J., 2012, *Astrophysics Source Code Library*, record ascl:1202.009
- Snedden C., Lucatello S., Ram R. S., Brooke J. S. A., Bernath P., 2014, *ApJS*, 214, 26
- Takeda Y., 2020, preprint (arXiv:2001.04588)
- Takeda Y., Hashimoto O., Taguchi H., Yoshioka K., Takada-Hidai M., Saito Y., Honda S., 2005, *PASJ*, 57, 751
- Takeda Y., Omiya M., Harakawa H., Sato B., 2016, *PASJ*, 68, 81
- Thielemann F. K. et al., 2011, *Prog. Part. Nucl. Phys.*, 66, 346
- Tody D., 1986, in Crawford D. L. ed., SPIE Conf. Ser. Vol. 627, Instrumentation in Astronomy VI. SPIE, Bellingham, p. 733
- Tsantaki M., Delgado-Mena E., Bossini D., Sousa S. G., Pancino E., Martins J. H. C., 2023, *A&A*, 674, 157
- Tsuji T., 2008, *A&A*, 489, 1271
- Viscasillas Vázquez C. et al., 2022, *A&A*, 660, A135
- Wallace L., Livingston W., 2003, NSO Technical. Rep. 03–001, An atlas of the solar spectrum in the infrared from 1850 to 9000 cm<sup>-1</sup> (1.1 to 5.4 micrometer). National Solar Observatory, Tucson, AZ
- Wilson J. C. et al., 2019, *PASP*, 131, 055001
- Womack K. A., Vincenzo F., Gibson B. K., Côté B., Pignatari M., Brinkman H. E., Ventura P., Karakas A., 2023, *MNRAS*, 518, 1543
- Yuk I.-S. et al., 2010, in McLean I. S., Ramsay S. K., Takami H. eds, SPIE Conf. Ser. Vol. 7735, Ground-based and Airborne Instrumentation for Astronomy III. SPIE, Bellingham, p. 77351M
- Zacharias N., Finch C. T., Girard T. M., Henden A., Bartlett J. L., Monet D. G., Zacharias M. I., 2013, *AJ*, 145, 44

## APPENDIX A: EXTRA MATERIAL

**Table A1.** Analysed lines and atomic and molecular parameters were used to determine the abundance values. The abundance values obtained after applying NLTE correction are indicated in parentheses.

Specie	$\lambda$ (Å)	$\chi$ (eV)	log $gf$	$gf$ Source	log $\varepsilon(X)$			
					#14	#43	#50	#60
C ( <sup>12</sup> C <sup>16</sup> O)	23 109.370	1.512	−4.907	Goorvitch (1994)	8.03	8.21	7.90	7.73
	23 122.094	1.549	−4.900	Goorvitch (1994)	8.04	8.21	7.89	7.73
	23 303.581	1.421	−4.517	Goorvitch (1994)	8.11	8.22	7.95	7.58
N ( <sup>12</sup> C <sup>14</sup> N)	23 304.591	0.485	−4.994					
	15 321.421	1.051	−1.959	Snedden et al. (2014)	7.87	7.68	7.89	7.95
	15 321.424	0.791	−1.755					
	15 410.558	0.840	−1.555	Snedden et al. (2014)	7.92	7.74	7.92	7.97
	15 447.095	1.092	−1.160	Snedden et al. (2014)	7.92	7.72	7.97	7.94
	15 466.235	1.092	−1.154	Snedden et al. (2014)	7.90	7.70	7.96	7.98
	15 471.812	0.860	−1.708	Snedden et al. (2014)	7.88	7.60	7.91	7.93
O ( <sup>16</sup> OH)	15 481.868	0.863	−1.542	Snedden et al. (2014)	7.94	7.70	7.92	7.93
	15 391.057	0.494	−5.512	Brooke et al. (2016)	8.59	8.53	8.45	7.94
	15 391.205	0.494	−5.512					
	16 872.277	0.759	−5.032	Brooke et al. (2016)	8.58	8.52	8.40	8.04
	16 886.275	1.059	−4.720	Brooke et al. (2016)	8.52	8.56	8.43	8.02
	16 904.278	0.896	−4.712	Brooke et al. (2016)	8.56	8.48	8.43	7.98
	16 909.289	0.897	−4.712	Brooke et al. (2016)	8.62	8.66	8.54	8.13
F (H <sup>19</sup> F)	23 358.329	0.227	−3.962	Jönsson et al. (2014)	4.16	4.14	3.96	—
Na I	22 056.426	3.189	+0.290	Kramida et al. (2014)	6.37	6.01	6.29	5.90
	23 348.423	3.750	+0.280	Kramida et al. (2014)	6.38	6.06	6.36	6.00
	23 383.136	3.750	+0.530	Kramida et al. (2014)	6.31	5.97	6.23	5.93
	21 059.727	6.779	−0.384	Civiš et al. (2013)	7.41	7.40	7.35	7.31
Mg I					(7.30)	(7.31)	(7.24)	(7.21)
	21 060.710	6.779	−0.530	Civiš et al. (2013)	7.45	7.46	7.38	7.34
	21 060.896	6.779	−1.587		(7.32)	(7.34)	(7.24)	(7.21)
	21 060.896	6.779	−0.407					
	21 061.095	6.779	−3.383					
	21 061.095	6.779	−1.583					
	21 061.095	6.779	−0.298					
Al I	21 093.078	4.820	−0.400	Kramida et al. (2014)	6.42	6.35	6.46	6.05
					(6.25)	(6.19)	(6.29)	(5.89)
	21 163.800	4.820	−0.090	Kramida et al. (2014)	6.51	6.36	6.44	6.07
					(6.33)	(6.17)	(6.24)	(5.89)
Si I	15 960.080	5.979	+0.200	Kramida et al. (2014)	—	—	7.28	7.28
	16 060.009	5.949	−0.500	Afşar et al. (2018)	7.18	7.24	7.11	7.10
	16 094.797	5.959	−0.090	Afşar et al. (2018)	7.31	7.28	7.21	7.08
	16 215.691	5.949	−0.580	Kramida et al. (2014)	7.32	7.15	7.25	7.07
	16 241.851	5.964	−0.85	Afşar et al. (2018)	7.30	7.28	7.16	7.20
P I	16 482.920	7.207	−0.560	Afşar et al. (2018)	5.45	5.80	5.60	5.56

**Table A1** – *continued*

Specie	$\lambda$ (Å)	$\chi$ (eV)	log $gf$	$gf$ Source	log $\varepsilon(X)$			
					#14	#43	#50	#60
S I	22 507.597	7.870	−0.480	Afşar et al. (2018)	6.96	7.09	7.00	7.09
	22 519.106	7.870	−0.380	Afşar et al. (2018)	—	7.16	7.14	7.16
	22 526.052	7.870	−0.700	Afşar et al. (2018)	6.96	6.91	7.06	7.19
	22 563.868	7.870	−0.280	Afşar et al. (2018)	7.04	6.94	7.13	7.26
K I	15 163.090	2.668	+0.550	Afşar et al. (2018)	5.06	4.95	4.96	4.87
Ca I	16 136.823	4.528	−0.670	Afşar et al. (2018)	6.29	6.20	6.20	6.09
	16 150.762	4.529	−0.280	Afşar et al. (2018)	6.18	6.09	6.11	5.91
	16 155.236	4.529	−0.770	Afşar et al. (2018)	6.29	6.17	6.09	6.11
	16 157.364	4.551	−0.240	Afşar et al. (2018)	6.19	6.09	6.11	5.96
Sc I	22 065.232	1.438	−0.840	Pehlivan, Nilsson & Hartman (2015)	2.87	2.68	2.85	2.32
	22 266.729	1.427	−1.400	Pehlivan, Nilsson & Hartman (2015)	3.05	2.95	3.02	2.55
Ti I	17 376.577	4.486	+0.550	Afşar et al. (2018)	4.77	4.80	4.73	4.58
	17 383.103	4.472	+0.440	Afşar et al. (2018)	4.79	4.77	4.77	4.63
	21 782.944	1.748	−1.140	Afşar et al. (2018)	4.86	4.73	4.99	4.32
	22 211.238	1.732	−1.750	Afşar et al. (2018)	4.79	4.62	4.77	4.20
	22 232.858	1.738	−1.620	Afşar et al. (2018)	4.79	4.73	4.85	4.31
Cr I	15 860.210	4.693	+0.000	Afşar et al. (2018)	5.60	5.49	5.56	5.35
	17 708.730	4.385	−0.510	Afşar et al. (2018)	5.34	5.31	5.26	5.10
Fe I	15 343.788	5.649	−0.690	Afşar et al. (2018)	7.18	7.25	7.14	7.15
	15 858.657	5.583	−1.250	Afşar et al. (2018)	7.16	7.16	7.07	7.07
	17 420.825	3.879	−3.520	Afşar et al. (2018)	7.19	7.23	7.20	7.16
	21 284.348	3.069	−4.510	Afşar et al. (2018)	7.32	7.31	7.19	7.12
	21 735.462	6.170	−0.730	Afşar et al. (2018)	7.28	7.28	7.27	7.23
	21 851.381	3.639	−3.630	Afşar et al. (2018)	7.23	7.24	7.20	7.08
	22 419.982	6.213	−0.300	Afşar et al. (2018)	7.22	7.14	7.07	7.16
	23 308.478	4.073	−2.730	Afşar et al. (2018)	7.18	7.17	7.18	7.05
Ni I	16 673.706	6.030	+0.100	Afşar et al. (2018)	6.03	6.06	5.95	5.98
	16 815.472	5.301	−0.590	Afşar et al. (2018)	5.91	5.89	5.86	—
	16 818.745	6.035	+0.330	Afşar et al. (2018)	5.96	5.91	5.95	—
	17 306.518	5.484	−0.530	Afşar et al. (2018)	5.91	—	—	—
Ce II	16 376.480	0.122	−1.790	Cunha et al. (2017)	1.53	1.62	1.34	1.22
	16 595.230	0.122	−2.190	Cunha et al. (2017)	1.58	1.66	1.39	1.28
Nd II	16 053.628	0.745	−2.200	Hasselquist et al. (2016)	1.30	1.35	—	—
	16 262.043	0.986	−1.990	Hasselquist et al. (2016)	1.50	1.65	1.54	1.48
Yb II	16 498.396	3.020	−0.380	Afşar et al. (2018)	0.78	1.00	0.85	0.91

This paper has been typeset from a  $\text{\TeX/L\AA\TeX}$  file prepared by the author.